Measurements, Analysis and Modelling of the Vibrations of a Tyre by Using a Single Embedded Accelerometer

Jaakko Laine

School of Electrical Engineering

Thesis submitted for examination for the degree of Master of Science in Technology.

Espoo 10.10.2016

Thesis supervisor:

Prof. Arto Visala

Thesis advisor:

M.Sc. (Tech.) Arto Niskanen

Aalto University
School of Electrical
Engineering

AALTO UNIVERSITY
SCHOOL OF ELECTRICAL ENGINEERING

ABSTRACT OF THE
MASTER'S THESIS

Author: Jaakko Laine

Title: Measurements, Analysis and Modelling of the Vibrations of a Tyre by Using a Single Embedded Accelerometer

Date: 10.10.2016 Language: English Number of pages: 7+71

Department of Electrical Engineering and Automation

Professorship: AS-84 Automation Technology

Supervisor: Prof. Arto Visala

Advisor: M.Sc. (Tech.) Arto Niskanen

Tyre vibration measurements and analysis for static and rolling tyres have been conventionally performed using complex sensor configurations. In this thesis, methodology for performing similar measurements and analysis using a single accelerometer system is presented.

An accelerometer was attached to the inner side of the tyre treadband and the tyre was excited with a hammer or a cleat in the static and rolling cases respectively. Using data from multiple measurements, complete records of treadband accelerations were reconstructed, sets of tyre modes identified and a flexible ring tyre model parametrised.

The results from the static cases provided good agreement with the theory, while the rolling cases were difficult to validate despite high measurement resolution and approximate agreement with the tyre model.

Keywords: tyre vibration, tyre model, vibration measurement, modal analysis, SSI, FRF

AALTO-YLIOPISTO
SÄHKÖTEKNIIKAN KORKEAKOULU

DIPLOMITYÖN
TIIVISTELMÄ

Tekijä: Jaakko Laine

Työn nimi: Renkaan värähtelyn mittaus, analyysi ja mallinnus yhdellä renkaaseen asennetulla kiihtyvyysanturilla

Päivämäärä: 10.10.2016 Kieli: Englanti Sivumäärä: 7+71

Sähkötekniikan ja automaation laitos

Professuuri: AS-84 Automaatiotekniikka

Työn valvoja: Prof. Arto Visala

Työn ohjaaja: DI Arto Niskanen

Rengasvärähtelyn mittaamiseen ja analyysiin liikkumattomasta ja erityisesti vierivästä renkaasta on tavallisesti käytetty monimutkaisia useamman sensorin mittausjärjestelyjä. Tässä diplomityössä esitellään menetelmiä vastaavien mittausten tekemiseen käyttäen vain yhtä kiihtyvyysanturia.

Värähtelyitä mitattiin renkaan sisäpintaan kiinnitetyllä kiihtyvyysanturilla, ja rengasta herätettiin joko vasaran tai dynamometrin rumpuun kiinnitettävän esteen avulla. Toistokokeiden mittausarvoista onnistuttiin työssä koostamaan koko renkaan vyön kiihtyvyysarvot, tunnistamaan renkaan moodit ja parametroimaan flexible ring -rengasmalli.

Liikkumattomaan renkaaseen liittyvien mittauksien tulokset sopivat hyvin yhteen teorian kanssa, mutta vierivän renkaan mittaustuloksien varmentaminen oli haastavaa huolimatta mittausten korkeasta resoluutiosta ja yhteensopivuudesta parametroidun mallin kanssa.

Avainsanat: rengasvärähtely, rengasmalli, värähtelymittaus, moodianalyysi, SSI, FRF

Preface

The measurements performed in this thesis were carried out in the laboratory of the Vehicle Engineering Research Group at Aalto University, during the years 2015-2016. I am grateful for all the support I got while working in the laboratory.

I would like to express my gratitude to my instructor M.Sc. (Tech.) Arto Niskanen for his help in the measurement instrumentation and for the feedback I got during the thesis work. I would also like to thank my supervisor Prof. Arto Visala for his support and confidence in this work.

Otaniemi, 10.10.2016

Jaakko T. K. Laine

Contents

Symbols and abbreviations

Symbols

$H_i(\omega)$	frequency response function
$\Gamma_i(\omega)$	coherence function
$S_{FX_i}(\omega)$	averaged cross spectral density
$S_{X_iX_i}(\omega)$	averaged auto spectral density of the response
$S_{FF}(\omega)$	averaged cross spectral density of the input
ω	angular velocity
ξ	damping ratio
A_n	amplitude of a peak in the FRF
A_{hpp}	amplitude of a peak's half power point in the FRF
A	state matrix of a system
C	output matrix of a system
x	state vector of a system
y	measurement vector of a system
v and w	Gaussian white noise
Q, S and R	Covariance matrices
Λ	output covariance matrix of a system
Σ_0	state covariance matrix of a system
G	next state-output covariance matrix of a system
$H_{p,q}$	block-Hankel matrix with p block rows and q block columns
O_p	observability matrix of a system
C_q	controllability matrix of a system
N_m	number of system modes
ψ_i	ith eigenvector of a matrix
Δt	time interval between two samples
λ_i	discrete time system pole of a system
λ_{ci}	continuous time system pole of a system
ϕ_i	mode shape related to ith system pole
m	mass of the wheel
R	radius of a tyre
k_v	tangential spring stiffness of the flexible ring
k_w	radial spring stiffness of the flexible ring
k_2	stiffness of the secondary spring in the flexible ring model
b	width of a tyre
h	thickness of the ring in the flexible ring model
τ	thickness of the secondary spring in the flexible ring model
EI	bending stiffness of the flexible ring
ρ	density of the ring in the flexible ring model
b	width of a tyre
I_r	moment of inertia of the wheel
n	circumferential mode number of a mode
a	cross-sectional mode number of a mode

A_c	area of the cross-section of the flexible ring in the flexible ring model
p_0	the air pressure of the tyre
H	section height of a tyre
f	frequency of a wave
k_θ	circumferential wave number of a wave
v_p	phase velocity of a wave
v_g	group velocity of a wave
k_θ	circumferential wave number of a wave
f_n	natural frequency of the tyre
L_c	length of the tyre air cavity
v_{air}	speed of sound in air
λ	wave length of a wave

Operators

A^T	transpose of a matrix A
δ_{pq}	Kronecker delta
$E[]$	expectation operator
$A^\uparrow$	upper shifted matrix of A defined by multiplication with an upper shift matrix
A^{-1}	the inverse of matrix A
$\times$	cross product of two vectors
$\frac{\mathrm{d}}{\mathrm{d}t}$	derivative with respect to variable t
$\sum_i$	sum over index i

Abbreviations

EMA	experimental modal analysis
FRF	frequency response function
SSI	stochastic subspace identification
LDV	laser Doppler vibrometer
ESC	electronic stability control
ABS	anti-lock braking system
IEPE	integrated electronic piezoelectric
ADC	analog to digital converter

1 Introduction

The dynamic behaviour of rubber pneumatic tyres have been studied extensively for decades [1, 2, 3]. Because the forces and moments affecting a car have to transmit through the tyres of the car, it is essential to understand the interactions between them and the road surface. Deflection in the tyre gives rise to forces and vibrations that can either be attenuated or magnified depending on the frequency range of the vibration. In general, the materials and structure used in the manufacturing of a modern radial ply passenger car tyre dampen the high frequency vibrations more than the low frequencies, this causes the tyre to act as a low pass filter for road irregularities.

The frequencies amplified by the tyre are called its natural frequencies. The natural frequencies can vary depending on the construction and materials used in the manufacturing of the tyre. However, the natural frequencies can also change during operation. The most important parameters related to the shifting of natural modes are the road contact type, the rotation speed and the inflation pressure of the tyre. Vibrations in the tyre are generally undesired because they increase the noise generated by the tyre [4, 5]. Dynamic analysis of tyre behaviour can be used to design more silent tyres as was presented by Iwao et al. in 1996 [5].

More recently some research has been focused on tyre sensors as a part of the active safety system of a car [6, 7, 8, 9]. Analysing the vibrations of the tyre rubber with corotating accelerometers could allow estimation of the available friction, predictive slip detection and estimation of the contact forces.

In previous research the modal analysis of a tyre is often performed with multiple sensors attached to the treadband [3] or by using a laser Doppler vibrometer standing next to the tyre [10]. The results of these experiments have been used to create tyre models that try to predict and explain the tyre modes.

Many different types of tyre models with varying explanation power have been presented starting from simple two-dimensional models to highly complicated three-dimensional finite element models. In this thesis we focus on the two-dimensional flexible ring model presented by Gong in 1993 [1], because using a single corotating accelerometer only allows us to measure the in-plane vibrations of the tyre. The flexible ring model also provides a high explanation power at frequency ranges below 300 Hz while still remaining relatively easy to implement and parametrise.

Using only a single accelerometer is attractive because it greatly reduces the complexity and cost of the measurement configuration required when measuring a rotating tyre. Measuring a rotating tyre with an attached accelerometer is difficult because a slip ring is required to transmit the power and measurement signals to and from the tyre.

In this thesis the formation of tyre modes is discussed, methods for detecting the tyre modes with a single embedded accelerometer are presented, the modes of a passenger car tyre are measured and identified using the methods presented and finally the flexible ring model presented by Gong is parametrised and compared to the measurements [1].

2 Methods of Analysis

In this section different methods for analysing tyre vibration are presented. This includes explanations on some of the algorithms used for detecting the modal parameters of tyres.

2.1 Experimental Modal Analysis

Experimental modal analysis(EMA) is used to describe the dynamic behaviour of a structure in terms of frequency, damping and mode shapes. Knowledge of the behaviour in the frequency domain is useful because all rigid structures exhibit the cyclic behaviour that can be found in combined spring-mass systems. The geometry and material choices result in attenuation or amplification of certain vibration frequencies in the structure.

Because the properties rise from geometry and material it is possible to do modal analysis either by modelling the system mathematically using the geometry and material information or directly measuring the behaviour of an existing system. These methods can also be combined to create more accurate representations of the system.

Most measurement driven methods of modal analysis rely on measurable excitation of the structure with an impact hammer or a shaker. By measuring the response of the system, the natural frequencies, mode shapes and damping can be determined. To find these parameters Fourier analysis is often used. In this thesis the tyre is excited with an impact hammer that provides a force input measurement. To estimate the mode shapes, multiple measurements are performed with different positions of the sensor inside the tyre.

2.2 Frequency Response Function

The measurements allow the calculation of the frequency response functions(FRF) that describe how the system reacts to a given input signal. The FRF operates in the frequency plane and is thus a tool of Fourier analysis. The FRF is calculated between an input and an output measurement. To model the whole tyre, multiple FRF measurements have to be used. To ensure similar excitation signals for multiple measurements a coherence function can be used and excitation signals differing too much discarded. The coherence function can also be calculated from the input and output signals. For the input the measured quantity is often the excitation force, but the output vibration can be displacement, velocity or acceleration. Velocity and acceleration measurements differ by a 90 degree phase shift in the measured FRF because of the phase shift between acceleration and velocity in a single degree of freedom oscillator.

The FRF $H_i(\omega)$ and coherence function $\Gamma_i(\omega)$ can be estimated with equations

[3]:

$$H_i(\omega) = \frac{S_{FX_i}(\omega)}{S_{FF}(\omega)} \tag{1a}$$

$$\Gamma_i(\omega) = \sqrt{\frac{|S_{FX_i}(\omega)|^2}{S_{X_iX_i}(\omega)S_{FF}(\omega)}}, \tag{1b}$$

where $S_{FX_i}(\omega)$, $S_{X_iX_i}(\omega)$ and $S_{FF}(\omega)$ are the averaged cross spectral density, the auto spectral density of the ith response and the auto spectral density of the excitation signal [3].

2.3 Peak Picking Method

By using the FRF it is possible to determine the natural frequencies, damping and mode shapes of the system. One of the simplest methods for detecting natural frequencies is the so called peak picking method. In peak picking the natural frequencies are detected from the peaks of the FRF [11]. The natural frequencies should show up in most of the calculated FRFs. It won't appear in measurements corresponding to the zero magnitude position of the associated mode shape.

The modal damping can be estimated from the peak widths of the resonance peaks. Same frequency peaks should have the same width in the different FRFs. The width is measured at the half power point of the FRF peak, and is approximately equal to twice the modal damping [11]. As an equation this can be described as

$$\xi_n = \frac{|\omega_2 - \omega_1|}{2\omega_n} \tag{2}$$

where ω_2 and ω_1 are the frequencies of the half power points around the natural frequency ω_n. The position of the half power point can be identified by finding the point where the amplitude of the FRF is:

$$A_{hpp} = \frac{A_n}{\sqrt{2}} \tag{3}$$

where A_{hpp} is the amplitude at half power point and A_n is the amplitude at natural frequency.

The mode shapes for the detected natural frequencies can be determined with the quadrature method of curve fitting. For FRFs that have been created from acceleration or displacement measurements, the mode shape can be detected from the peak values of the imaginary parts of the FRFs taken as components of the mode shape [11]. For FRFs calculated from velocity measurements, the mode shapes are detected from the peak values of the real parts of the FRFs [11]. This difference is caused by the phase shift between acceleration and velocity.

The problem of the peak picking method is that it is highly subjective and produces only a coarse estimate of the natural frequency and damping if the system has heavy modal coupling. Additionally, determining the damping and mode shapes

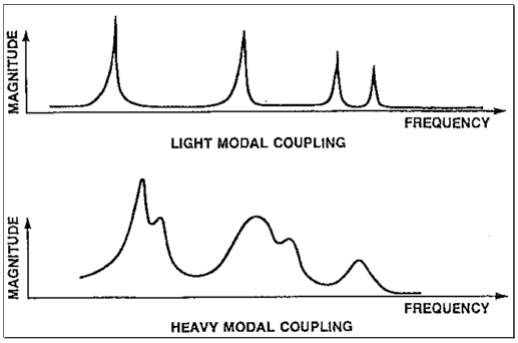

Figure 1: The difference between light and heavy modal coupling in the FRF. [11]

in complex structures with closely spaced modes becomes difficult. Examples of the FRFs of systems with light and heavy modal coupling are shown in figure 1. It is easy to see that determining the peak width from the heavily coupled FRF can prove difficult.

2.4 Stochastic Subspace Identification Method

The Stochastic Subspace Identification(SSI) algorithm is a method for data driven system identification that has been known to outperform the classical techniques [12]. It can be used to detect a linear time invariant state-space model that best explains the measurements made. From this model it is later possible to calculate the desired modal parameters with well known formulas. It is possible to find the natural frequencies, attenuations and mode shapes. The technique is relatively recent when compared to many frequency domain methods, and was first presented by Van Overschee & De Moor in 1991 [13]. It has later been improved [14, 15] and presented in more understandable form [12].

2.4.1 Stochastic State-Space Models

The state-space formulation that is used is of the form:

$$x_{k+1} = Ax_k + w_k \tag{4a}$$

$$y_k = Cx_k + v_k \tag{4b}$$

where $y_k \in \mathbb{R}^l$ is a measurement sequence generated by the system, $x_k \in \mathbb{R}^n$ is a state vector and $k = 0, 1, ..., K$ is the index of time step. System matrices A and C are the state space and output matrices respectively and model the effect of the previous state on the new state and new measurement. Equation 4a is therefore called the state equation and models the dynamic behaviour of the system. Similarly equation 4b is called the observation or output equation and details which components of the state are measured. The Gaussian white noise sequences $w_k \in \mathbb{R}^n$ and $v_k \in \mathbb{R}^l$ are assumed to be zero mean with covariance matrices Q, S and R defined as [12, 14]:

$$E\left[\begin{pmatrix} w_p \\ v_p \end{pmatrix}\begin{pmatrix} w_q^T & v_q^T \end{pmatrix}\right] = \begin{pmatrix} Q & S \\ S^T & R \end{pmatrix}\delta_{pq} \tag{5}$$

where E is the expectation, p and q denote the time step and δ_{pq} is the Kronecker delta function. It should be noted that the process noise w_k drives the system response while the measurement noise v_k is only due to sensor inaccuracies and doesn't affect the actual state of the system [12].

Next we define the output covariance matrices Λ_0 and Λ_i as [12, 15]:

$$\Lambda_0 = E[y_k y_k^T] \tag{6a}$$
$$\Lambda_i = E[y_{k+i} y_k^T] \tag{6b}$$

Because w_k and v_k are independent of the state vector x_k, we can establish the following properties from equations 4 to 6 [12, 15]:

$$E[x_k x_k^T] = A\Sigma_0 A^T + Q \tag{7a}$$
$$E[x_{k+1} y_k^T] = G = A\Sigma_0 C^T + S \tag{7b}$$
$$\Lambda_0 = C\Sigma_0 C^T + R \tag{7c}$$
$$\Lambda_i = CA^{i-1}G \tag{7d}$$

where Σ_0 is the state covariance matrix and G is the next state-output covariance matrix [12].

2.4.2 Identification of the System Matrices

If we can detect the system matrices A and C of the stochastic state-space model from the measurement data, we are able to determine the natural frequencies, dampings and mode shapes of the system. Multiple variant methods for finding the best matrices A and C have been presented in literature. We have chosen to present the Principal Component method [16], also known as the covariance-driven SSI algorithm, because it is relatively simple to implement and computationally not too demanding [12].

First a block-Hankel matrix filled with output covariance matrices Λ_i is defined [12]:

$$H_{p,q} = \begin{pmatrix} \Lambda_1 & \Lambda_2 & \dots & \Lambda_q \\ \Lambda_2 & \Lambda_3 & \dots & \Lambda_{q+1} \\ \vdots & \vdots & \ddots & \vdots \\ \Lambda_p & \Lambda_{p+1} & \dots & \Lambda_{p+q+1} \end{pmatrix} \tag{8}$$

The matrix $H_{p,q}$ has p block rows, q block columns and a well known factorisation property that can be derived from equation 7d stating that [12, 15]:

$$H_{p,q} = \begin{pmatrix} C \\ CA \\ \vdots \\ CA^{p-1} \end{pmatrix} \begin{pmatrix} G & AG & \dots & AG^{q-1} \end{pmatrix} = O_p C_q, \tag{9}$$

where $O_p \in \mathbb{R}^p$ and $C_q \in \mathbb{R}^q$ are the observability and controllability matrices respectively. They are assumed to be of rank $2N_m$, where N_m is the number of

system modes [12]. The matrices O_p and C_q can be determined by using a singular value decomposition on $H_{p,q}$ and the equation 9 as [12, 15]:

$$H_{p,q} = \begin{pmatrix} U_1 & U_2 \end{pmatrix} \begin{pmatrix} S_1 & 0 \\ 0 & 0 \end{pmatrix} \begin{pmatrix} V_1 \\ V_2 \end{pmatrix} = U_1 S_1 V_1^T = (U_1 S_1^{1/2})(S_1^{1/2} V_1^T) = O_p C_q \tag{10}$$

Here matrices U, S and V are the results of a singular value decomposition on $H_{p,q}$.

If $O_p^{\uparrow}$ is used to mark the upper shifted O_{p-1} matrix by one block row, it is possible to obtain [12, 15]:

$$O_p^{\uparrow} = \begin{pmatrix} CA \\ CA^2 \\ \vdots \\ CA^{p-1} \end{pmatrix} = O_{p-1} A, \tag{11}$$

from where it is easy to see that A can be solved by calculating $O_p^{\uparrow}$ and O_{p-1} from O_p. It is similarly easy to see from equation 9 that C is the first block row of matrix O_p. This only leaves the calculation of the covariance matrices Λ_i before we can solve the system matrices A and C.

After calculating the system matrix A, the modal parameters can be extracted from it. The first step is to calculate the discrete-time system poles λ_i and the corresponding right side eigenvectors ψ_i. This can be done with an eigenvalue decomposition of A [12, 15]:

$$A = \Psi \Lambda \Psi^{-1}, \tag{12}$$

where $A\psi_i = \lambda_i \psi_i$ and Λ contains the system poles on its diagonal. The continuous time poles are then related to discrete time system poles by [12, 15]

$$\lambda_{ci} = \frac{\ln(\lambda_i)}{\Delta t}, \tag{13}$$

where Δt is the time step between samples. The undampened eigenfrequencies f_i and damping ratios ξ_i in percentage form result from the system poles [12, 15]:

$$f_i = \frac{|\lambda_{ci}|}{2\pi} \tag{14a}$$

$$\xi_i = -100 \frac{\lambda_{ci}^R}{\lambda_{ci}}, \tag{14b}$$

where $\lambda_{ci} = \lambda_{ci}^R + i\lambda_{ci}^I$. The experimental mode shapes ϕ_i can be calculated by multiplying the eigenvectors ψ_i with the measurement matrix C [12, 15]:

$$\phi_i = C\psi_i, \tag{15}$$

2.4.3 Practical Considerations

An algorithm for detecting the modal parameters of a system based on measurements can be created by using the equations of the previous section. Here we present some points related to a practical implementation of an algorithm based on SSI.

It should be noted that all the previous developments were made for systems with finite system order and exact block-Hankel matrices. In reality the exact output covariance matrices are unknown and a mechanical system has an infinite system order [12]. Regardless, it is possible to calculate an unbiased estimate $\hat{\Lambda}_i$ of the covariance matrices forming the block-Hankel matrix [12, 15]:

$$\hat{\Lambda}_i = \frac{1}{N-1} \sum_{k=0}^{N-i-1} (y_{(k+i)} y_k^T), \tag{16}$$

where $0 \leq i < N-1$ and N is the number of observations.

Using singular value decomposition on the approximate block-Hankel matrix result in [12, 15]:

$$\hat{H}_{p,q} = \begin{pmatrix} \hat{U}_1 & \hat{U}_2 \end{pmatrix} \begin{pmatrix} \hat{S}_1 & 0 \\ 0 & \hat{S}_2 \end{pmatrix} \begin{pmatrix} \hat{V}_1 \\ \hat{V}_2 \end{pmatrix} \tag{17}$$

Because the real model order is infinite and the block-Hankel matrix is only an approximation, the matrix $\hat{S}_2$ is not a zero matrix as in equation 10. Therefore the most fitting model order has to be determined. If too low model order is selected, multiple mode shapes can combine and be mistaken for true mode shapes. On the other hand, too high model order can result in mode shapes being fitted to the random variation in the measurement data. This also results in incorrect modes being detected.

The correct model order can sometimes be determined by comparing the singular values of equation 17. Because the singular values correspond to the amount of data covariance explained by the modes, the correct model order can in some cases be detected from a big drop in the explanation power of additional model dimensions. If it is not possible to easily identify a good model order based on the singular values, a stabilization diagram can be drawn [17]. This is often the case in modal analysis, because the correct model order of a system is infinite.

2.5 Stabilization Diagram

A stabilization diagram is plotted when identifying a system to find the correct model order is difficult. It is especially useful in structural dynamics, where the order of the models is typically chosen very high to reduce the bias on the estimates and capture all of the relevant characteristics of the structure, even in the presence of large amounts of measurement noise [17]. The consequence of overspecification is that the physically meaningful poles are detected along a set of mathematical poles without any relation to the structural problem [17].

To plot a stabilization diagram the system is first identified with a wide range of model orders. After the modal parameters have been calculated for all of the identified models, the natural frequencies are plotted in a diagram with frequency on the horizontal and model order on the vertical axis. The stabilization diagram can therefore visualize all of the identified models in a way that is still relatively readable and includes some information about the identified modes. Experience on a large range of problems shows that the physical poles always appear at a nearly

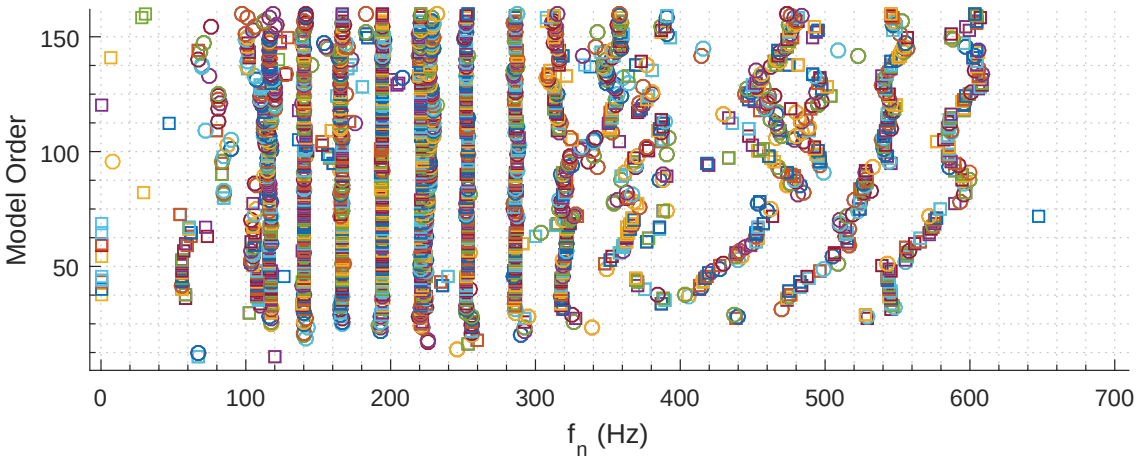

Figure 2: A stabilization diagram for a static tyre using squares for frequencies with stable frequency and damping. Circles are used to mark poles with stable frequency but unstable damping.

identical frequency, while mathematical poles tend to scatter around the frequency range [12, 17, 18]. Because the physical modes of the structure should be the same regardless of identification method, it seems natural that the spurious frequencies can't describe a physical property of the structure. However, it should be noted that insufficiently excited modes can sometimes be mistakenly classified as spurious modes [17].

Optionally the natural frequencies of the system can be drawn with different symbols to indicate the stability of the detected mode. This is done by comparing the identified modal parameters to the ones provided by the lower order models. In this thesis the modal parameters compared for stability are frequency and damping. The criteria used were:

- If the natural frequency identified is within 1% of the one detected by the previous model, the frequency is considered stable
- If the damping identified is within 5% of the one detected by the previous model, the damping is considered stable

The symbols used for marking the stability of the detected poles in this thesis are written as follows: If the frequency and damping are both stable, the frequency is marked to the stabilization diagram with a small square. If only the frequency is stable, it is marked with a circle. If neither of the two are stable or only the damping value is stable, the natural frequencies are not plotted to the diagram. A stabilization diagram using these symbols is shown in figure 2.

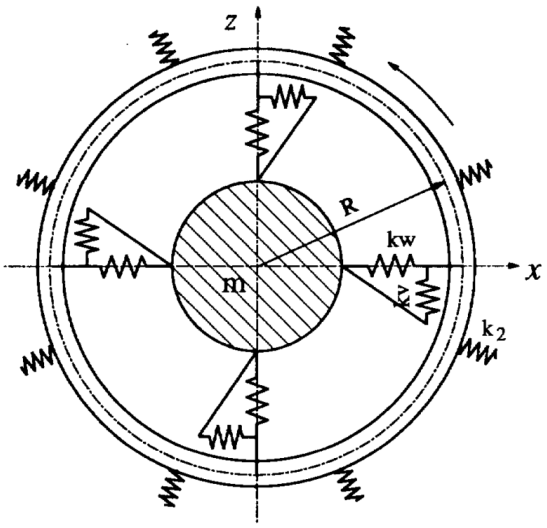

Figure 3: The flexible ring model with radial springs for modeling the tread pattern. [1]

2.6 The Flexible Ring Tyre Model

The flexible ring tyre model is a two-dimensional tyre model in which the treadband is modelled as an elastic ring. The side walls and the air cavity are presented as a group of radial and tangential springs that support the treadband. Additionally for studying the tyre-road contact problem, additional springs outside the treadband can be added to model the elasticity of the tyre tread rubber. More advanced and complex three-dimensional finite element models(FEM) are generally more powerful than the flexible ring models in predicting the vibrations of the tyre, but they can also be more difficult to create and parametrise. Therefore, in this thesis we only consider the flexible ring model. The version of the model chosen for this thesis is the one introduced by Gong in 1993 in his PhD thesis [1]. The flexible ring model has also been studied by Kim in 1997 and Zegelar in 1998 [2, 3].

2.6.1 Parameter Estimation

The parameters of the flexible ring model can be divided into three categories: geometric, stiffness and inertial parameters [1]:

- The geometric parameters include: the radius R, the width b, the thickness h of the ring, and the thickness τ of the secondary spring.
- The stiffness parameters include: the stiffness of radial springs k_w, the stiffness of the tangential springs k_v, the stiffness of the secondary spring k_2 and the bending stiffness of the ring EI.
- The inertial parameters include: the density of the ring ρ, the mass of the wheel m and the moment of inertia of the wheel I_r.

The geometric parameters of the tyre ring model can either be measured or obtained from the tyre geometries. The inertial parameters can be approximated similarly by measuring the mass of the wheel, the mass of the rubber and calculating the moment of inertia based on the masses and radii. Correctly approximating the inertial parameters is, however, made more complicated by the exclusion of the tyre walls from the model. The mass of the rubber walls has to therefore be accounted for in the mass of the rim or in the mass of the rubber. The division of the sidewall mass can therefore affect the results of the simulation. One possible solution is to add half of the mass of the sidewall to the mass of the rim and half to the mass of the treadband as was done by Zegelaar in 1998 [3]. If the mass is divided this way, half of the sidewall is considered to move with the rim and half with the treadband.

The stiffness parameters of the tyre can be approximated either by theoretical analysis or tyre tests[1]. The former requires some information on the Poisson's ratio and other properties of the rubber. The latter is performed by measuring the natural frequencies of a static tyre and then determining the radial, tangential and bending stiffnesses by using the equations for the tyre natural frequencies. These frequencies for a static tyre with fixed wheel under the in-extensibility assumption are given by Gong as [1]:

$$\omega_n = \left\{ \frac{1}{\rho A_c (1+n^2)} \left[\left[\frac{EI}{R^4} \left(1-n^2\right) - \frac{p_0 b}{R} \right] n^2 \left(1-n^2\right) + k_v + k_w n^2 \right] \right\}^{\frac{1}{2}}, \tag{18}$$

where $n = 0, 1, 2, ..., +\infty$ is the circumferential mode number, ρ is the density of the treadband, A_c is the area of the cross-section of the ring, R is the radius of the ring, p_0 is the air pressure of the tyre, b is the width of the ring, EI is the bending stiffness, k_v is the tangential spring stiffness and k_w is the radial spring stiffness. Because the only values that need to be determined from measurements in equation 18 are the stiffness parameters, if we measure three natural frequen0cies of a tyre, we can then solve the bending, radial spring and tangential spring stiffness. The other detected natural frequencies can then be used for model validation.

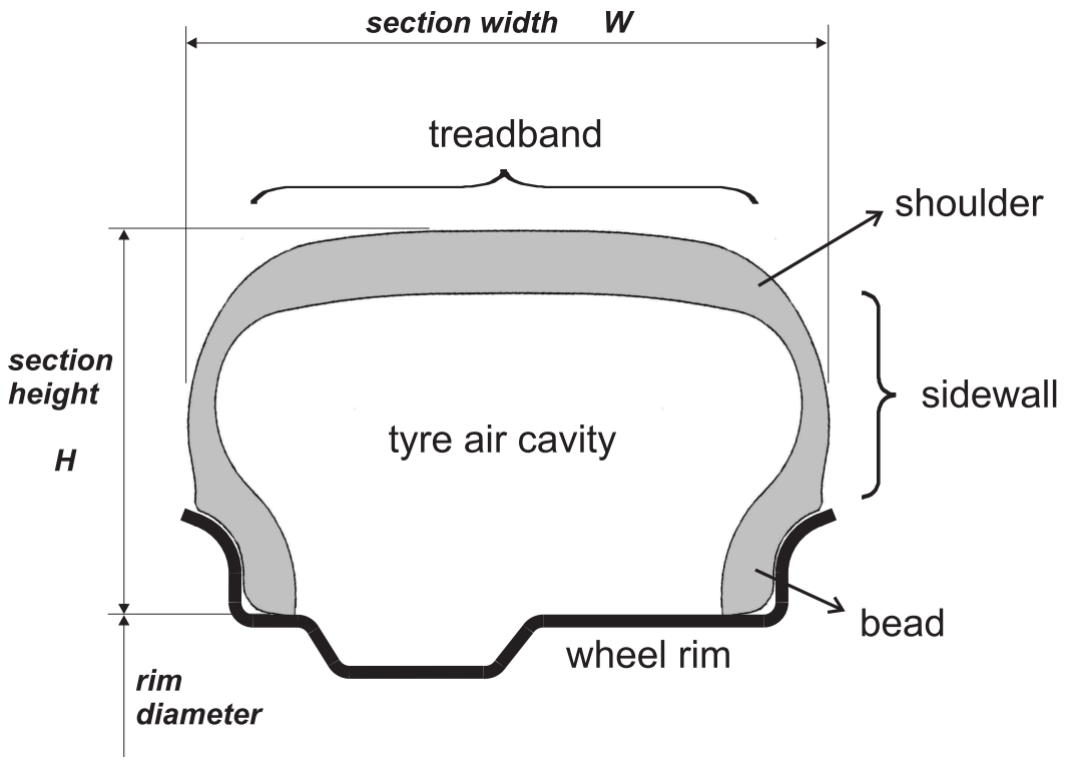

Figure 4: Cross-section of a tyre-wheel assembly. [10]

3 Tyre Vibration

Vibrations of nonrotating structures have been studied for a long time. A rubber tyre is not an exceptionally complex vibrating system and can be analysed by the traditional methods of modal analysis. However, the system becomes harder and more difficult to analyse once the tyre starts to rotate and the centrifugal, Euler and Coriolis forces start affecting the tyre. In a rotating tyre it is also much harder to install the required instrumentation for measuring the vibrations of the tyre. Depending on the sensor used one may also have to consider the Doppler shift of detected frequencies. Additionally the ground contact patch can apply a changing local strain on the tyre and restrain its movement in the area of ground contact. It can also break the otherwise perfect symmetry between the left and right side of the excitation point.

In this section the structure of a rubber tyre and some of the theory behind tyre vibration is presented. The vibrations of an unloaded tyre are considered in two cases: a static tyre mounted with bolts from the wheel and a rotating tyre without ground contact. Finally the effect of the contact is considered on both of these cases. Measuring the vibration of the rubber belt is also considered. The differences between a corotating and a static measurement device are presented.

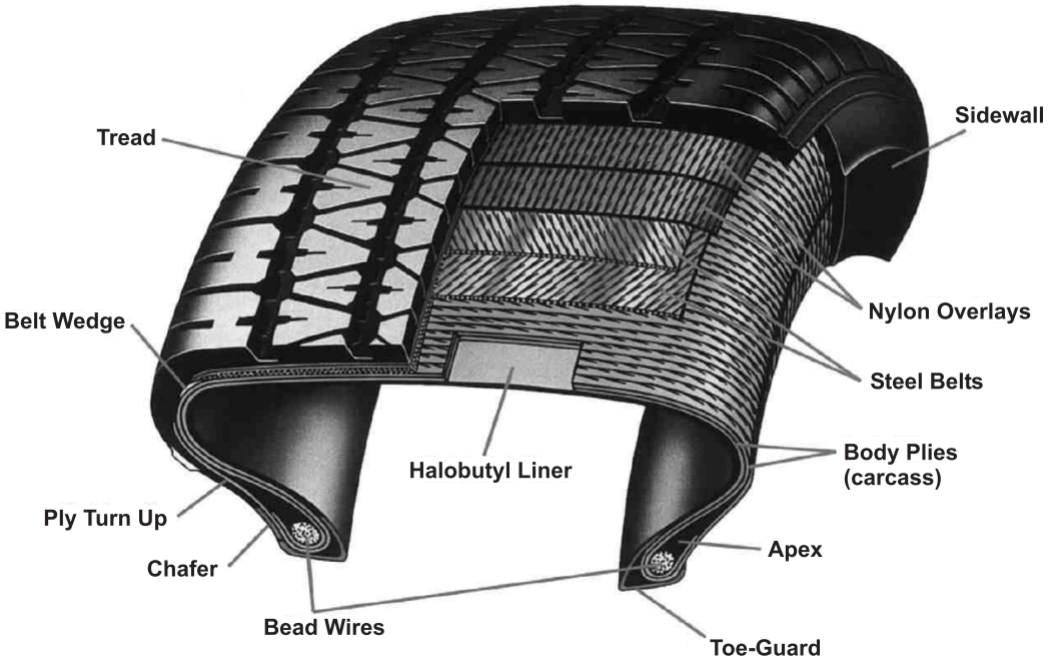

Figure 5: Construction of a radial ply tyre. [19]

3.1 Tyre Structure

A modern car wheel consists of a metal rim and a tyre. The tyre is pressurised with air, but it doesn't have an inner tube. Instead, the air is trapped between the tyre and the rim. This makes it easier to attach an accelerometer to the inner side of the tyre treadband. The different portions of the tyre are named in a cross-sectional view of a tyre and a rim at figure 4.

The tread and outer layer of a car tyre consist of many different substances and materials used may depend on the manufacturer. A construction of a radial ply tyre can be seen in figure 5. The materials can be divided into three major categories:

- **Fabric:** steel, nylon, aramid fibre, rayon, fibreglass, polyester, kevlar
- **Rubber:** natural and synthetic
- **Additives:**
  - reinforcing chemicals: carbon black, silica resins
  - anti-degredants: antioxidants/ozonants, parafin waxes
  - curatives: cure accelerators, activators, sulfur
  - processing aids: oils, softeners [10]

It is good to keep in mind that the structure of the tyre can be nonlinear whenever trying to express the behaviour of the tyre with a linear model. Therefore linear

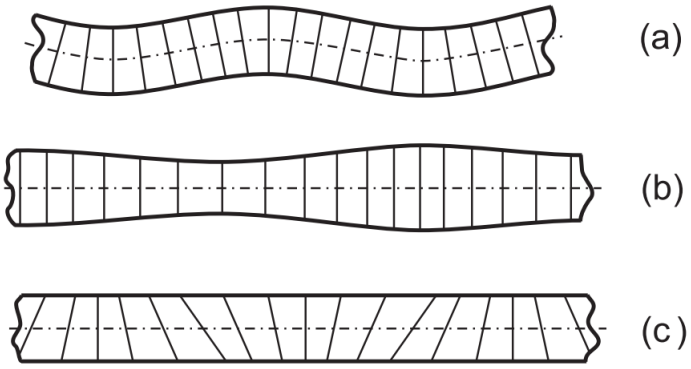

Figure 6: The three wave types propagating in the tyre treadband: (a) bending wave, (b) longitudinal wave, (c) rotational wave. [10]

models give good results only when the rubber operates under its linear operating conditions. The figures 4 and 5 should be used as reference to the terminology used when discussing the different parts of the tyre in this thesis.

3.2 Classification of Tyre Vibration and Mode Shapes

It has been noted by Kindt that: "There is no standardised way of labelling tyre modes. This leads quite often to misunderstandings in discussions and interpretations of results in publications." [10] Therefore the labelling introduced by Kindt in 2009 is adopted and briefly presented in this paper [10]. The labelling is based on the one by Wheeler et al. in 2005 for an unloaded tyre [20].

In the treadband of a tyre, three different types of circumferentially propagating waves in the frequency range under 3 kHz, can be identified [21, 22]: **bending**, **longitudinal** and **rotational** waves. The deformation of the treadband for all of the three wave types is shown in figure 6. From these deformation types it is possible to see that the bending waves result mainly in radial displacement of the belt and the longitudinal waves cause mainly tangential displacement of the belt. It should also be possible to detect the rotating waves with an accelerometer attached to the inner surface of the tyre, but differentiating them from the longitudinal waves might prove difficult. Nevertheless, the propagation speed of the rotational wave is much higher than other wave types and has a cut on frequency around 2500 Hz [21]. Therefore it is possible to ignore them if we are only interested in the low frequency vibrations and modes of the tyre(0 - 500 Hz).

The properties of rubber cause an increase in the attenuation of vibrations with increasing frequency in a tyre. This is due to the well known viscoelastic properties of the tyre rubber [10]. The loss factor of rubber increases with frequency while working at the rubbery region. This region for unfilled natural rubber at room temperature extends from 0 to about 5000 Hz [10]. This results in modal behaviour of the tyre with low vibration frequencies. With frequencies over 500 Hz the tyre doesn't show much modal behaviour, because the waves emitted from the excitation decay too

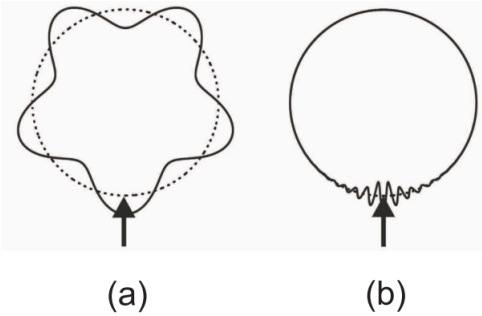

Figure 7: Structural behaviour of a tyre: (a) Low frequency modal behaviour. (b) High frequency non-modal behaviour. [10]

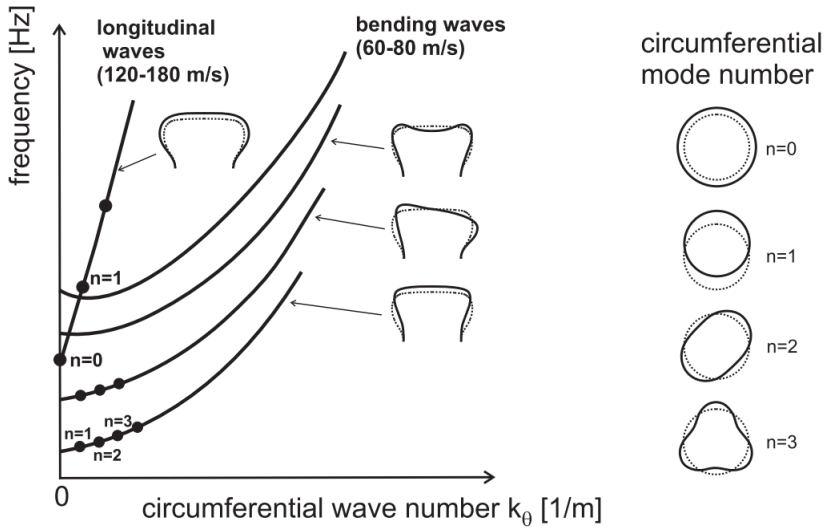

Figure 8: Typical tyre dispersion curves for bending and longitudinal waves. [10]

fast to cause any meaningful constructive interference [22]. The structural behaviour of the tyre is presented at figure 7.

In addition to the circumferential vibration, the tyre can also vibrate in the cross-sectional view. This is why the tyre vibration mode shapes are not completely explained if considering only the circumferential shape of the modes. Theoretically for each circumferential mode shape there should exist an infinite number of cross-sectional deformation shapes as illustrated in figure 8. It should also be noted that the 0th mode of the tyre is caused by longitudinal waves. This is significant because the cross-sectional shape affects the frequency and propagation speed of the mode [10]. In practice, the detectable mode shapes are limited by the attenuation of the high frequencies in rubber, but it is still possible to detect multiple mode shapes with the same circumferential mode number. The group velocity of the wave with a given wave number can be calculated from the tangent of the dispersion curve as follows [10]:

$$v_g = 2\pi \frac{df}{dk_\theta} \tag{19}$$

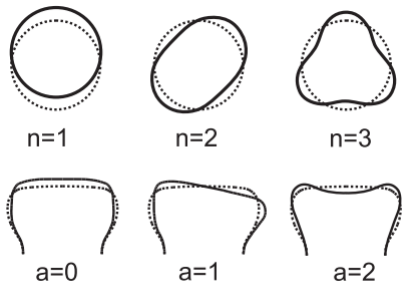

Figure 9: Labelling of the tyre structural modes (n, a), where n = circumferential index and a = belt cross-sectional index. as presented by Kindt in 2009. [10]

The phase velocity can also be determined from the dispersion curve because it gives the relation between angular velocity ω and wavenumber k_θ [10]:

$$v_p = \frac{\omega}{k_\theta} \tag{20}$$

The end result is that each mode has at least the following properties:

1. **Wave type:** Bending, longitudinal or rotational wave.
2. **Circumferential shape:** Expressed by index, $n = 1, 2, 3, ...$
3. **Cross-sectional shape:** Expressed by index, $a = 0, 1, 2, ...$
4. **Natural Frequency:** Visible as a peak in the tyre spectrum.
5. **Damping:** The rate of attenuation for the frequency in the tyre.

The notation for the mode shapes of an unloaded tyre presented by Wheeler et al. uses the circumferential and cross-sectional indexes and implicit knowledge of the wave type [20]. The format of the notation is (n,a) and the two letters represent the circumferential and cross-sectional index as explained above. Example mode shapes of the labelling can be seen in figure 9.

The circumferential index n represents the number of circumferential bending wavelengths of the belt and is also called the circumferential mode number [10]. The cross-sectional index a represents the number of half-wavelengths in the axial direction of the treadband at a circumferential location, where the shape is at an extreme radial displacement [10]. This notation has been extended by Kindt to better cover the modes of a loaded tyre [10]. The two number notation for mode shapes is ambiguous for some of the modes in which the belt translates or rotates as a rigid structure [10]. For those modes an alternative label, such as: **"axial"** and **"torsional"**, is used to indicate the rigid body movement of the belt [10].

An unloaded tyre is axisymmetric. Therefore, most of its system poles in the frequency plane are double and form complex conjugate pairs. These complex poles correspond to the waves travelling around the tyre and the combinations of the

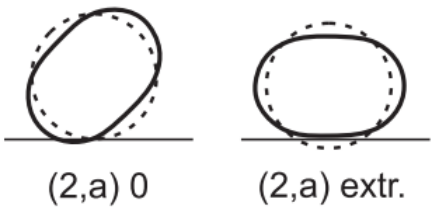

Figure 10: Examples for the (2,a) modes of the loaded tyre using the additional labels **"0"** and **"extr"** as defined by Kindt. [10]

complex conjugates form standing waveforms. However, when the tyre is loaded the symmetry breaks, which causes a split of the double poles of the unloaded tyre into two single poles [10]. Because both of the modes are related to the same mode of the unloaded tyre, an additional distinction between them is required. The labelling provided by Kindt specifies the following additional labels based on an observed trend [10]:

- Label **"0"** is added for the mode with radial displacement of zero in middle of the tyre/road contact area.
- Label **"extr"** is added for the mode with an extremum of the radial displacement in the middle of the tyre/road contact area.

An example of these two labels applied in the case of the (2,a) modes of the loaded tyre are presented in figure 10. This labelling is still ambiguous for some of the modes where the belt translates or rotates as a rigid structure. Therefore, another label was added by Kindt [10]:

- For the $(1, 1)$ and $(1, 0)$ modes the label **"vert"** translates along the vertical tyre axis.
- For the $(1, 1)$ and $(1, 0)$ modes the label **"hort"** translates along the horizontal tyre axis.

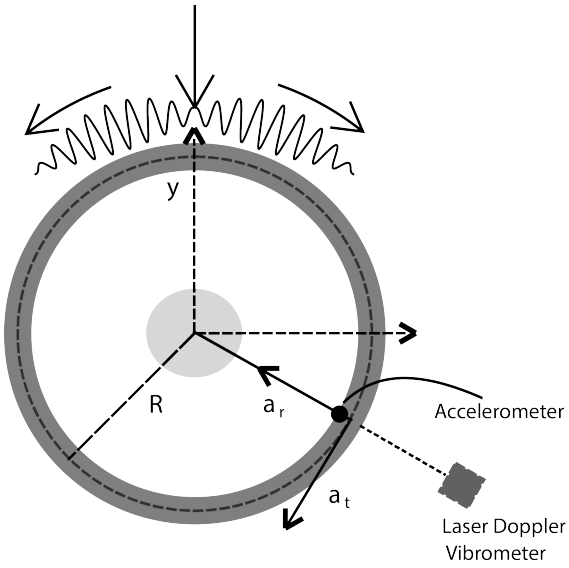

Figure 11: A static tyre showing point excitation and vibration measurement with an accelerometer and a laser Doppler vibrometer.

3.3 Static Tyre

A static tyre is here defined as a tyre that is connected from the centre of the rim, so that the rim is not allowed to rotate or move freely. In this section the tyre has no ground contact and the rubber portion is free to vibrate. This makes it possible to analyse the vibration of the tyre separate from the suspension, ground contact and rotation speed. The behaviour of the static tyre, however, depends significantly on the inflation pressure of the tyre. The pressure applies load, pretensioning the tyre and affecting its modes.

Modal testing for a static tyre is usually performed as an impact test. In a test like this the tyre is struck with an impact hammer, which sends impulses containing a wide range of frequencies rotating around the tyre as can be seen from figure 11. The different frequencies in the impulses are attenuated or amplified depending on the properties of the tyre. By measuring the vibration with a laser Doppler vibrometer (LDV) or an accelerometer one can determine the natural frequencies by the methods of experimental or operational modal analysis. Additionally it is possible to calculate the group velocity v_g with equation

$$v_g = \frac{2\pi R}{t_{cycle}}, \tag{21}$$

where R is the radius of the tyre and t_{cycle} is the round trip time of the impulse.

There are some differences between an LDV and an accelerometer for measuring the vibration of the tyre treadband. Some of the most notable differences are listed as follows:

- A three-axis accelerometer can measure tyre vibration in all directions while an LDV can't easily measure it in the tangential direction.

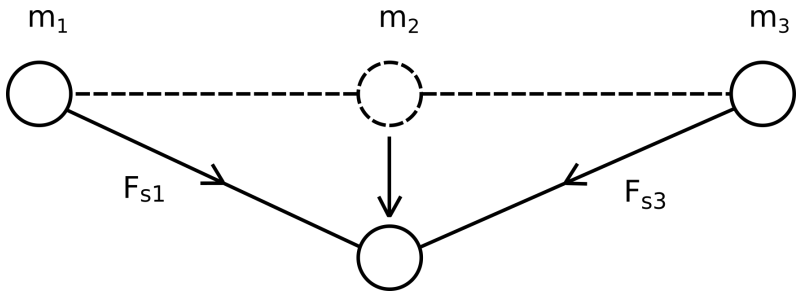

Figure 12: The displacement of m_2 causing forces F_{s1} and F_{s3} on masses m_1 and m_3.

- An accelerometer measures acceleration, while an LDV measures velocity.
- An accelerometer may add a significant point mass to the measured system and cause a roving mass effect, while an LDV affects the measured tyre very little.
- An accelerometer rotates with the tyre, while an LDV stands stationary next to the tyre.
- An accelerometer can measure vibration also in the tyre ground contact patch.
- An accelerometer mounted inside a tyre can be relatively easily used for measuring tyre vibration on real driving conditions, while an LDV can't easily be used outside the laboratory.
- An accelerometer can measure vibration inside the tyre, while an LDV measures the outer edge of the tyre.
- An accelerometer attached to the treadband of the tyre can turn when the treadband bends, which makes the acceleration vectors measured to rotate out of alignment, when compared with the basis vectors of the cylindrical coordinate system, while an LDV always measures the velocity in the same direction.

In the case of a static tyre the impulses will travel with equal speed around the tyre meeting at the opposite side. This will cause an interference of the two propagating waves and result in the formation of standing waves in the tyre. If the tyre is excited in the radial direction, most of the vibration in the tyre will happen in that direction, but some vibration will also be detected in the circumferential direction. Tangential vibration will be there even if the excitation is perfectly radial because displacement in the radial direction will cause a spring force with both components as shown in figure 12. This means that the radial and tangential vibrations are somewhat coupled in a standing tyre.

The standing waves formed in the tyre are identified as two complex conjugate poles in the pole-zero plot of the system. The complex conjugate poles correspond to mode shapes with an additional imaginary component which are interpreted as shapes rotating around the tyre. This makes sense because it means that the mode

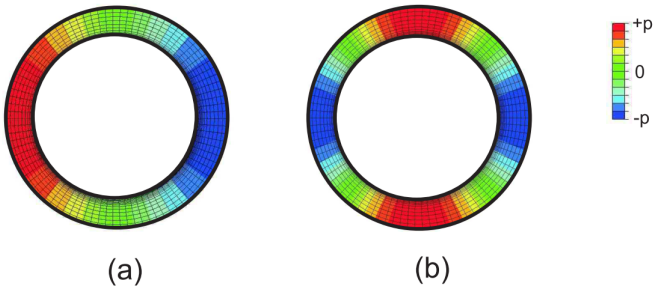

Figure 13: The first two modes of the air cavity resonance with red depicting positive and blue negative pressure: (a) the first mode the of air cavity resonance, (b) the second mode of the air cavity resonance. [10]

shapes rotate around the tyre like the travelling waves. The mode shapes are complex conjugates of each other like the system poles. Therefore, the shape of the standing wave can also be found by summing the complex conjugate mode shapes. It is easy to see that the sum of the two rotating mode shapes results in a standing wave because the imaginary values of complex conjugates disappear when the complex numbers are summed. Almost all poles of a static tyre are detected double because of the axisymmetry of the tyre.

The modes of the tyre structure explain most of the modes detected when measuring the acceleration of the tyre tread band. Nevertheless, the pressure variations inside the tyre air cavity can also be detected by a sufficiently accurate measurement device. These pressure waves propagate inside the tyre forming cavity resonances, and are caused by the vibrations of the treadband. The modes of the cavity and the treadband are partially coupled and can affect each other [10]. Therefore, perfect modelling of the vibrations of the treadband would also have to consider the frequencies amplified by the air cavity of the tyre.

The first cavity resonance of an unloaded passenger car tyre form around 200 - 250 Hz [10]. The air cavity of an undeformed tyre can be modelled as an unwrapped torus to estimate the cavity resonance frequencies [23]. By assuming the tyre structure to be rigid and the wave inside the tyre planar, it is possible to calculate the resonance frequencies as [10]:

$$f_n = n\frac{v_{air}}{L_c}, \tag{22}$$

where n is the mode number, v_{air} is the sound velocity in the air cavity and L_c is the length of the air cavity. This kind of model should be accurate enough to predict the first two cavity resonance frequencies of the static tyre [10]. These two resonances are visualised in figure 13.

3.4 Rotating Tyre

In this section we consider a rotating tyre without ground contact. While it is still relatively simple to understand the vibrations of a static tyre, the situation gets much more complicated when the tyre starts to rotate. This additional complexity is mostly due to fictitious forces generated in non-inertial reference frames. In addition, the Doppler effect has to be taken into account when the measurement device moves in relation to the vibration source. The three fictitious forces in non-inertial reference frames are the **Centrifugal force**, the **Coriolis force** and the **Euler force**. If m is the mass of a particle, $\vec{\Omega}$ is the angular velocity of the coordinate system, $\vec{r}$ is the position vector of the particle starting from the centre of rotation and $\vec{v}_r$ is the velocity of the particle, the equations for these three forces are:

$$\vec{F}_{Centrifugal} = -m\vec{\Omega} \times (\vec{\Omega} \times \vec{r}) \tag{23a}$$

$$\vec{F}_{Coriolis} = -m\vec{\Omega} \times \vec{v}_r \tag{23b}$$

$$\vec{F}_{Euler} = -m\frac{d\vec{\Omega}}{dt} \times \vec{r} \tag{23c}$$

The Euler force only has an effect while the rotation speed of the reference frame changes. In tyre research a constant velocity of the tyre is often assumed and therefore the effect of the Euler force is not considered. The centrifugal force affects the tyre by increasing radial outwards load on the rubber ring. From equation 23a, it is possible to see that the stress caused by the centrifugal force increases quadratically when the rotation speed of the tyre increases. When this increased stress is combined with the Coriolis effect a rotational stiffening of the tyre results [24]. This increases the propagation speeds of the bending waves in the tyre [25]. However, the change in the speeds of the longitudinal and rotational waves due to this stiffening is essentially negligible [25].

The Coriolis force causes all velocity vectors presented in a rotating reference frame to rotate opposite to the rotation direction of the frame. This effect can increase the coupling between the radial and circumferential vibrations and cause a break in the symmetry of the waves travelling in different direction around the tyre. This is especially the case with fast rotation speeds of the tyre.

The result of the Coriolis acceleration is that the circumferential phase speeds of the forward and backward travelling waves differ even in the local rotating coordinates of the tyre [25]. In the global fixed coordinate system an opposing effect is caused by the Doppler shift, which causes the phase speed of the forward propagating wave to increase by the treadband tangential speed and the phase speed of the backward propagating wave to decrease by the same amount [25].

When observed from the rotating coordinate system and excited with a corotating force source, the result is that an excitation at a specific frequency produces two travelling waves with different phase speeds and same frequency. Because the relationship between the wave number k_θ, frequency ω and phase speed v_p is given by equation 20, the wave numbers have to differ for the different propagation directions. A wave moving around a rotating tyre is shown in figure 14. Therefore, the phases of the waves will never match at all points of the tyre and the interference of the

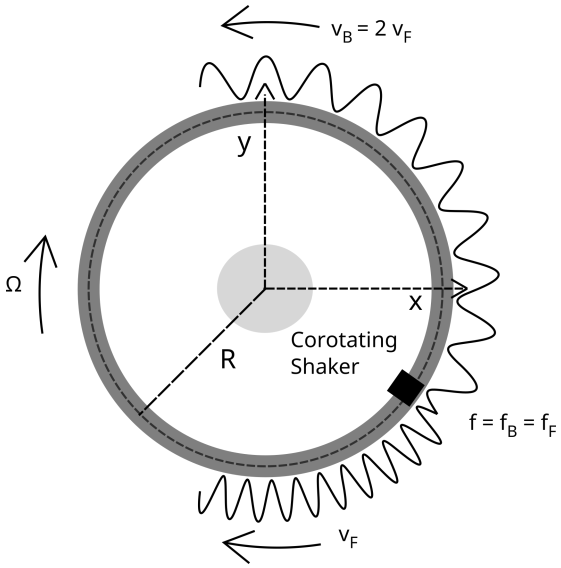

Figure 14: The travelling waves caused by a corotating shaker. Both waves have the same frequency, but travel at different velocities. The difference in propagation speed has been magnified to illustrate the travelling waves better.

waves will not produce a superposing standing wave. However, they will form an interference pattern, where the phase difference between the interfering sine waves changes along the tyre, but stays the same when fixed in space.

When the situation is instead considered from the perspective of a constant wave number and equation 20, we can see that the frequency of a wave with a constant wave number has to change with the phase speed. Therefore, the natural frequencies of a mode with a fixed circumferential mode number will change when the rotation speed of the tyre changes. Because a static tyre has the same phase speed for waves propagating in different directions, the waves produce a standing wave if the excitation is continued long enough. In a rotating tyre the waves will not produce a standing wave, because the frequencies of the waves corresponding to the same wave number don't match like in a static tyre. This causes the double poles of the tyre to split and form two single poles with different frequencies. This splitting of natural frequencies is known as the bifurcation effect [10]. It could be said that the Coriolis force breaks the physical symmetry of the rotating tyre even though the geometrical symmetry is still intact. This breakage of symmetry results in the aforementioned bifurcation of the natural frequencies.

We should also consider the interference of the propagating waves with themselves when travelling multiple laps around the tyre. A propagating wave interferes constructively or destructively with itself if

$$k_\theta = \pi n L, \tag{24}$$

where k_θ is the angular wave number, L is the length of the tyre circumference and $n = 1, 2, 3, ...$ When n is even, the interference is constructive, and when n is odd, the interference is destructive. The wave numbers fulfilling this equation correspond

to the mode shapes of the natural frequencies or anti-resonances. There are four possible cases when applying a continuous single frequency forced excitation:

1. Neither wave interferes constructively or destructively with itself.
2. The forward wave interferes constructively or destructively with itself ($k_f = 2\pi n_f L$).
3. The backward wave interferes constructively or destructively with itself ($k_b = 2\pi n_b L$).
4. Both waves interfere constructively or destructively with themselves, but with different wave numbers ($k_f = 2\pi n_f L$ and $k_b = 2\pi n_b L$).

The first three cases are much more common and produce either a single rotating mode shape or no mode shapes. The fourth case is only possible when the rotation velocity matches the excitation frequency so that equation 24 is satisfied for both of the waves. In this case there are two different rotating mode shapes or anti-resonances with the same natural frequency. If both of the waves resonate constructively with themselves, the end result would be a standing wave of sorts, but with the shape of the combined interference wave of the two mode shapes. This special case should be quite rare and next we will try to explore the conditions required for it to manifest.

The natural frequencies of a tyre under the inextensional assumption were given by Kindt in 2009 as [10]:

$$\omega_{n1} = \frac{2n}{n^2+1}\Omega + \sqrt{\omega_{fn}^2 + \frac{n^2(n^2-1)^2}{(n^2+1)^2}\Omega^2} > 0 \tag{25a}$$

$$\omega_{n2} = \frac{2n}{n^2+1}\Omega - \sqrt{\omega_{fn}^2 + \frac{n^2(n^2-1)^2}{(n^2+1)^2}\Omega^2} < 0, \tag{25b}$$

where n is the circumferential mode number, Ω is the rotation speed of the tyre, ω_{fn} is the natural frequency of the static tyre, ω_{n1} is the angular frequency of the backward travelling wave and ω_{n2} is the angular frequency of the forward travelling wave. Under the assumption of inextensible belt, the tangential vibration modes are excluded. If the natural frequencies of the static tyre are known, we can calculate the frequencies and velocities in which waves with differing wave numbers will form a standing wave. The static wave will form if $\omega_{l1} = -\omega_{k2}$, where l and k are the circumferential mode numbers and $l < k$.

In practice it may be very hard to detect multiple mode shapes with the same natural frequency because high frequencies are attenuated fast by the rubber and big differences in forward and backward wave numbers of the same frequency require very high rotation velocities for the tyre. It may also bee hard to detect the bifurcation of the natural frequencies in a rotating tyre, as it was concluded by Kim and Bolton in 2004, that the effect of rotation on the phase speed is essentially negligible at normal driving speeds [25]. The changes in the observed phase speed and frequencies caused by the Doppler effect and the Coriolis force were also compared in the same paper

by Kim and Bolton, and from their work it can be concluded that the Doppler effect has a significantly higher impact on the observed phase speed than the Coriolis force [25]. If vibration of the tyre is measured in the fixed coordinate system, the Doppler effect causes the frequencies to shift as shown in the equation below [10]:

$$(\omega_{nk})_{fixed} = \omega_{nk} - n\Omega, \tag{26}$$

where n is the circumferential wave number, $k = 1$ corresponds to the backward travelling wave observed at a lower frequency and $k = 2$ to the forward travelling wave observed at a higher frequency.

The most important conclusions on the effects of rotation on a tyre with no ground contact are summed up below:

1. A rotating tyre is subject to **Coriolis force** and **Centrifugal force**. The Centrifugal force causes increased load on the tyre rubber and the Coriolis force causes the circumferential speed of forward and backward travelling waves to differ.

2. The phase speed differences between waves of equal frequency make the formation of standing waves, between waves with the same wave number, impossible. This will result in complex valued mode shapes with different natural frequencies rotating around the tyre. This splitting of natural frequencies and double poles is called the **bifurcation effect**. In the corotating reference frame the mode shape associated with a backward travelling wave has a higher frequency than a forward travelling mode shape of the same wave number. However, standing waves can now form between modes of different wave numbers at specific rotation velocities. Despite all this, the relatively small differences in propagation speeds caused by tyre rotation at typical velocities make the whole bifurcation effect caused by rotation essentially negligible and hard to detect with measurements.

3. The waves travelling around the tyre are observed with a **Doppler shifted** frequency and a different rotation speed when measured from a fixed coordinate system. The difference in observed phase speed and wave number caused by the coordinate transformation is much higher than the effect caused by the Coriolis acceleration.

4. The phase speed of all bending waves will increase due to the rotational stiffening caused by the **Centrifugal** and **Coriolis** forces. However, the other wave types are essentially unaffected.

3.5 Ground Contact

Ground contact has a big effect on the modal behaviour of a tyre. Contact with the ground restricts the movement of the tyre treadband because of the friction between the rubber and the road surface. Additionally, the tyre deforms when it is pushed against the road by the weight of the vehicle. The deformation of the treadband and

the restrictions applied by friction break the axial symmetry of the tyre and cause the double poles of the unloaded tyre to split into two single poles [10].

The experimental work done to measure the tyre-road contact areas and contact distributions was summarised by Gong in 1993 as follows [1]:

1. The contact length between the tyre and the road is mostly determined by the tyre deflection. For constant tyre deflection, the contact length remains effectively constant when the load and inflation pressure change simultaneously.

2. The increase of rotating speed generally tends to increase the contact length slightly for a given normal load and inflation pressure.

3. Increasing the rotating speed causes an increase of contact pressure in the front part of the contact area and a decrease in the rear portion of the contact area.

4. For small normal loads, the distribution of pressure along the contact patch is a convex curve with the maximum pressure at the centre of the contact area. At high normal loads, the pressure distribution has a dip at the centre of the contact area.

If the tyre rotates while in ground contact, the contact patch can itself be considered an excitation source for the tyre. The preferred contact type for a rotating tyre is for it to roll on the road without slipping. When the tyre is perfectly rolling on the road the rotation speed Ω and the tyre forward velocity v_x are related by the equation [3]:

$$v_r = \Omega r_{eff}, \tag{27}$$

where r_{eff} is the effective rolling radius of the tyre. It was explained by Zegelaar et al. in 1998 that the effective rolling radius of the tyre depends on the tyre load, road plane angle, road curvature and the angle between the horizontal velocity v_x and the tyre velocity tangential to road surface v_t [3].

Because the tyre is the only part of the vehicle in contact with the ground and most of the forces affecting the vehicle are transmitted through them, it has become relevant to detect the loss of grip as soon as possible. None of the current commercial Electronic Stability Control(ESC) or Anti-lock Braking Systems(ABS) are based on sensors measuring the treadband even though the tyre is the part of the car with the fastest response to the changes in the contact patch.

The ground contact and high acceleration peaks of the rotating tyre make measuring the vibrations and deflections of the tyre contact patch hard. It is very difficult to measure the tyre deflections and vibrations with an external device because the ground blocks the view of optical measurement devices. On the other hand, the high shocks experienced by embedded measurement devices require high durability and very strong attachment to the tyre rubber.

Some solutions for measuring the contact patch deflections of the tyre have been studied: Tuononen used a light emitting diode(LED) and a two-dimensional position sensitive detector for measuring the deflections of the treadband in 2008 [7]. Matsuzaki and Todoroki studied different methods for tyre strain measurement

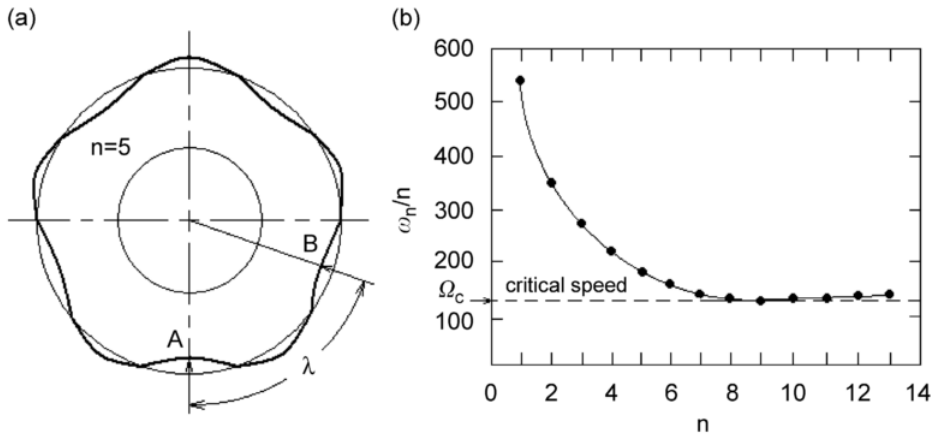

Figure 15: Illustrations for the critical speed: (a) the resonance condition and (b) the critical speed in the undampened case. [29]

and their usage for optimized braking control and road condition warning systems [8, 26, 27]. Very recently Niskanen and Tuononen used three durable three-axis integrated electronic piezoelectric (IEPE) accelerometers installed side by side to detect hydroplaning and perform tyre friction estimation [6, 28].

If the tyre deflection at the contact patch of a rolling tyre is observed from the rotating tyre coordinates, the contact patch seems to travel around the tyre deflecting the treadband. If the contact patch is then considered to be a rotating vibration source emitting travelling waves around the tyre, it should be clear that the frequencies of the travelling waves are subject to Doppler shift. Because the contact patch is considered as the moving sound source and the frequency detected at the rotating accelerometer the static observer, the equations for the forward and backward frequencies of the emitted frequency become:

$$f_F = \frac{c_{f_0}}{c_{f_0} + v_{wheel}} f_0 \tag{28a}$$

$$f_B = \frac{c_{f_0}}{c_{f_0} - v_{wheel}} f_0, \tag{28b}$$

where f_B is the frequency of the backwards travelling wave, f_F is the frequency of the forwards travelling wave, v_{wheel} is the forward velocity of the wheel, f_0 is the emitted frequency and c_{f_0} the phase speed of the travelling wave. Because rubber is a dispersive medium, the propagation speed of the emitted wave depends on its frequency. Additionally, as discussed in section 3.4 the phase velocity also depends on the rotation speed Ω of the tyre.

It should be noted that the equation predicts that the backwards frequency $f_B \to \infty$ if $(c_{f_o} - v_{wheel}) \to 0^+$. This corresponds to the contact patch breaking the sound barrier of the rubber tyre. Because the phase speeds for the different frequencies are different in the tyre, the barrier can not be broken at once. The dispersive media should produce a wide barrier starting and ending at specific velocities. Because all of the travelling waves don't contribute to the sound barrier effect at the same time,

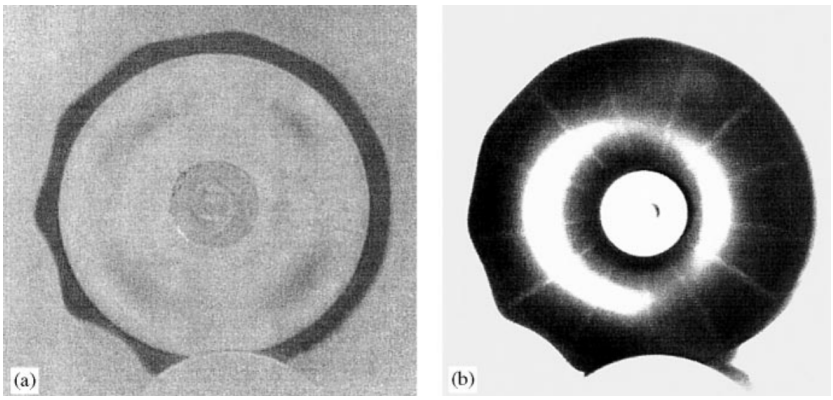

Figure 16: Clockwise rotating balloon tyres after the onset of standing waves: (a) Overlay of images taken at rest and above the critical speed showing the magnitude of tyre deformations and an increase in the contact patch area. (b) Image taken with a strobe showing that a white radial line on the tyre stays approximately straight as it rotates. [31]

the peak torque required to accelerate through the standing wave cut-on frequency should be lower than in a non-dispersive medium. This effect is closely related to the maximum velocity of the car tyre called the critical speed. This rolling speed for a tyre in the undampened case can be predicted by finding the minimum of the resonance condition [30]

$$\Omega_c = (\omega_n/n)_{min}, \tag{29}$$

where Ω_c is the critical rotation speed of the tyre, ω_n is the rotation speed of the nth mode and n is the mode number. The resonance condition is derived based on the fact that the tyre falls into resonance with the backward travelling mode shape when the contact force travels from A to B in the same time as the period of $t = 2\pi/\omega_n$ as illustrated in figure 15 [29].

The critical velocity represents a serious performance limitation for high speed vehicles, because at the critical frequency the tyre experiences an abrupt increase in the total strain energy, the heat generation and rolling resistance [31, 29]. The increase is big enough to not only cause a significant decrease in the fuel economy of the vehicle, but will also result in a tyre structural failure within minutes [29]. These effects are caused by a formation of a high amplitude standing wave at the critical speed [31, 29]. A small balloon tyre rotating past its critical speed is shown in figure 16. By experimenting with a thin balloon tyre Chatterjee et al. detected in 1999 that the standing wave phenomenon doesn't disappear after the critical speed has been reached [31].

Even though this kind of tyre deformation is being talked as standing waves in the cited literature, the difference between actual standing waves and these deformation patterns is that in a standing wave the nodal points are the only places with no movement. In the standing waves that form as a result of reaching the critical speed, the shape of the tyre doesn't change at any point of the tyre circumference when viewed from the non-rotating global coordinate system. Therefore, it would be much

better to talk about the constant deformation shapes, instead of using the term "standing wave". It is later shown by measurements in section 4.2 that this kind of static deformation pattern arises even much before the critical speed when the tyre is only excited by non-changing ground contact. However, the amplitude of the deformation shape is much smaller and impossible to detect by eye before the critical speed is reached. This might also help explain why the deformation pattern doesn't disappear after the critical speed has been reached.

4 Measurements and Results

In this thesis four types of tyre vibration measurements are considered. The goal is to determine the modes of the chosen tyre with a single embedded accelerometer in the following situations:

1. In the first experiment measurements are performed on a static tyre. The tyre has no ground contact and has been fixed in place with bolts from the rim. To get measurements from multiple positions around the tyre with a single accelerometer, the excitation is repeated multiple times and the tyre rotated from one position to another. The tyre is excited by a small impact hammer with a force sensor. To get more reliable result every position can be measured multiple times, failed excitations resulting in significantly different vibrations can be removed and the results from the acceptable excitations can be averaged.

2. In the second experiment the tyre is tested with ground contact. The tyre is attached to a system imitating the suspension of a car and pressed against the ground by a hydraulic cylinder. The excitation is produced by the impact hammer also used in the first experiment.

3. In the third experiment the tyre is tested with rolling ground contact. The tyre is rotated by driving it on a computer controlled steel drum. The excitation is produced by the rolling ground contact.

4. For the fourth experiment a cleat is attached to the rotating drum to simulate a road surface discontinuity and provide additional excitation for the rotating tyre. The vibrations of the tyre are then measured by the accelerometer rotating with the tyre. The moment the cleat contacts with the tyre is measured by attaching a permanent magnet near the cleat and detecting the cleat arrival point with a hall sensor.

Because we are only using a single accelerometer to measure the modes of the tyre, the cross-sectional indexes of the modes can not be differentiated. In all of the experiments the cross-sectional index a of all detected modes is supposed to be zero, because the modes with $a = 1$ should have a node in the middle of the treadband. The inability to differentiate between the modes with different cross-sectional indexes is a clear weakness for a system that only uses a single accelerometer.

For the first two measurements the data analysis is later performed using two different methods to better validate the results. The last two measurements are performed without measuring the excitation force. Because the input force is not measured, it is not possible to calculate a frequency response function between the excitation force and the tyre surface acceleration. Nevertheless, it should still be possible to detect the modes of the tyre and identify a model describing the measured acceleration by using the SSI method.

An accelerometer used for measuring tyre vibration has to be able to detect very high low duration acceleration peaks and give reliable measurements at high

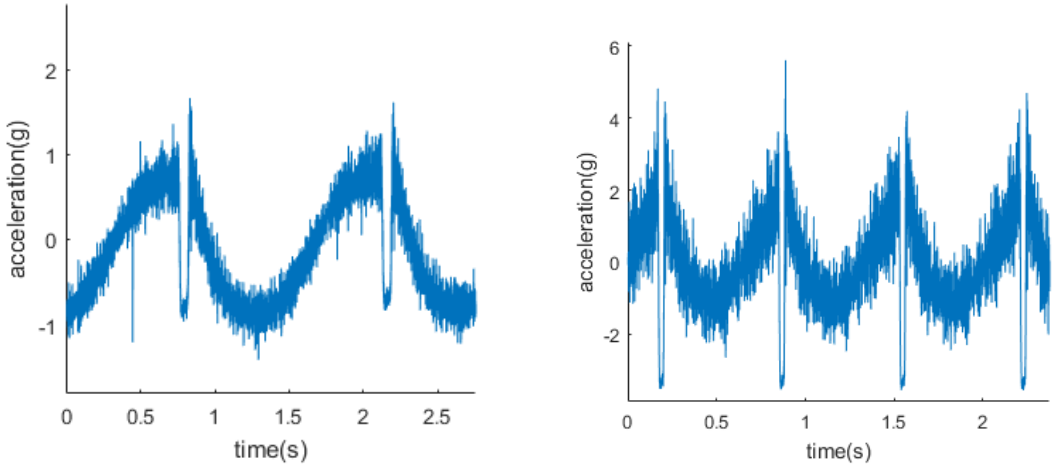

(a) Tyre rotating at a velocity of 5 km/h with a 4kN load.

(b) Tyre rotating at a velocity of 10 km/h with a 4kN load.

Figure 17: Preliminary measurements of the radial acceleration of a tyre rotating.

frequencies and sample rates. Because we are mostly interested in the high frequency tyre vibration, the low frequency performance of the sensor is not as important. To minimize the roving mass effect on the measurements the weight of the accelerometer should also be as low as possible. To measure the current angle of the rotating tyre and sensor an absolute encoder is attached to the rim of the tyre and the cabling can be routed out from the tyre with a slip ring.

To fill these requirements an integrated electronic piezoelectric(IEPE) accelerometer with a high resolution analog to digital converter(ADC) can be used. The model 35A Isotron® accelerometer by Endevco is a three-axis accelerometer providing a range of $\pm 1000g$ and a mass of 1.1 grams and is a good option for the presented scenarios [32]. However, it is necessary to note that the IEPE accelerometers act as a high pass filter. Therefore, it is not possible to detect constant acceleration and the real amplitudes and phases of low frequency accelerations can be significantly different from measured values. It is next shown that at the desired driving speeds the attenuation and phase shift of the low frequency vibrations are not very significant.

For the measurements of the static tyre the high pass filtering of the acceleration measurements means that the constant acceleration caused by the earth's gravitational field is invisible in the measurements. For a rotating accelerometer gravitational pull of the earth is visible, but the centrifugal force can not be seen as shown in figure 17a. From figure 17a it is also possible to see that the amplitude of the sine wave is only slightly reduced from the theoretical peak to peak value of 2g. From this it is possible to deduce that at the frequencies of the natural vibrations of the tyre, the amplitude error should not be an issue. The ground contact of the tyre can be seen as the negative acceleration spike in figure 17a. The time difference between the highest point of the sine wave pattern and the ground contact spike shows the phase shift caused by the high pass filter in the accelerometer. From figure 17b it is possible to see that the phase shift mostly disappears when the tyre is rolling at the

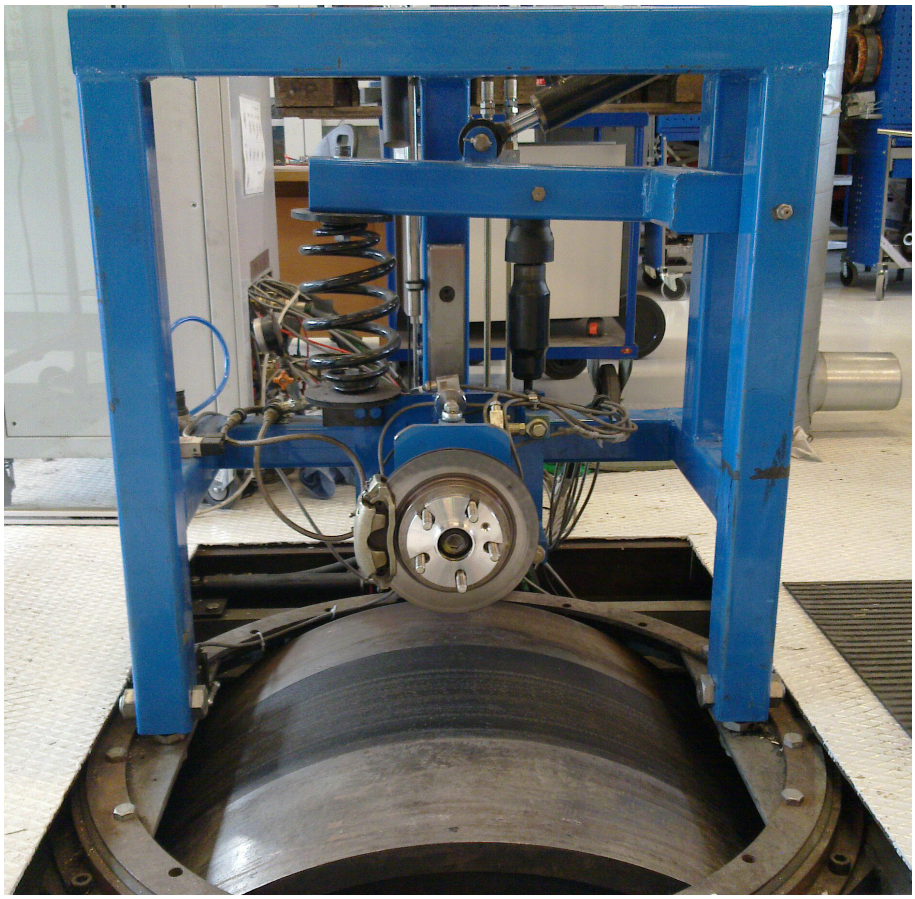

Figure 18: The tyre test bench in which all of the measurements of the thesis were performed.

speed of 10 km/h. Therefore, the phase shift of the measured vibrations should not be a problem at higher rotation velocities and vibration frequencies.

4.1 Measurement Setup

All of the measurements were performed in a tyre measurement bench designed by Pirjola and documented in his master's thesis in 2001 [33]. The measurement shown in figure 18, has been made to imitate the suspension of a car by using a spring and a damper. Additionally the hydraulic cylinder at the top of figure 18 allows the bench to apply a downwards force on the tyre to simulate the weight of a car.

The measured car tyre was a typical radial ply summer tyre with a marking 205/55R16 94H XL. The tyre also has a maximum allowed driving speed and load of 210 km/h and 670 kg respectively. From these tyre markings the following tyre dimensions can be deduced:

- The tyre width is 205 mm.
- The section height is 55% of the width resulting in a height of 112.75 mm.

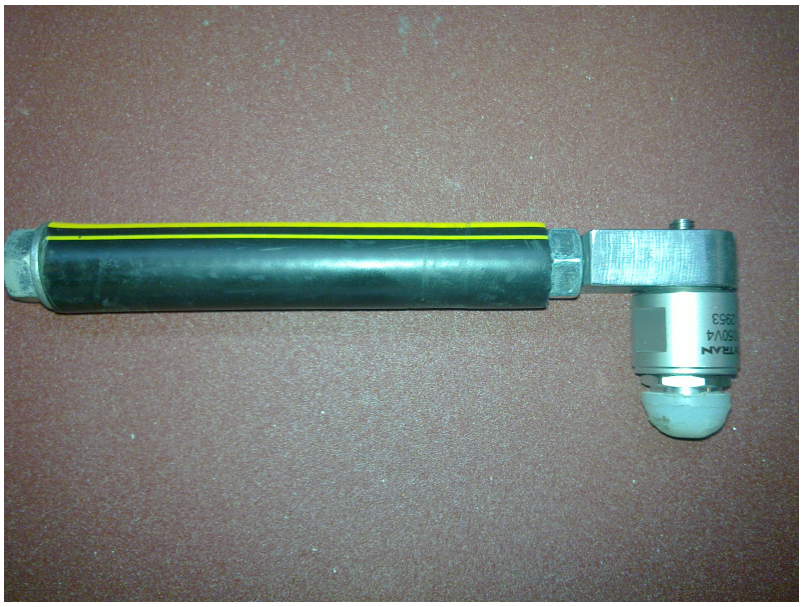

Figure 19: The impact hammer used in the measurements to excite the static tyre.

- The rim diameter is 16 inches or 406.4 mm.
- The calculated tyre diameter by using these numbers is therefore 631.9 mm. This seems to coincide well with our own measurement of 632 mm from a tyre with 2.2 bar pressure using two planes and a tape measure.

The drum seen in the bottom of the image is velocity controlled and can be used to rotate the car tyre. The drum has a four feet diameter which translates to 1.2192 meters. Additionally it has mounting holes to allow the installation of an aluminium cleat. The cleat can be used to excite the rotating tyre. For the experiments using the cleat excitation a magnet is installed into the side of the drum to detect the passing time of the cleat with a fast hall sensor.

In the first two measurements the excitation was applied with an impact hammer built from a force sensor, metal fittings and threaded rod. Additionally a plastic cover was attached on top of the threaded rod for user comfort and a round nylon head was attached to the force sensor. It was discovered that attaching a small flat aluminium piece at the tip of the nylon point made the excitation force higher and the duration shorter. Therefore, a small aluminium piece not shown in the pictures was used at the hammer tip. It was additionally discovered that there is a time delay between the measurement results from the accelerometer used in the tyre and the force sensor used in the hammer. This time delay was measured by striking the force sensor directly into the accelerometer. The time delay was then removed from the measurement data as a preprocessing step.

The aluminium cleat used for exciting the rotating tyre is shown in figure 20. The cleat was made from an aluminium bar by rounding the corners of the bar and drilling a hole on each end to attach the cleat to the two threaded holes of the drum. The corners of the cleat were rounded to decrease the horizontal movement of the

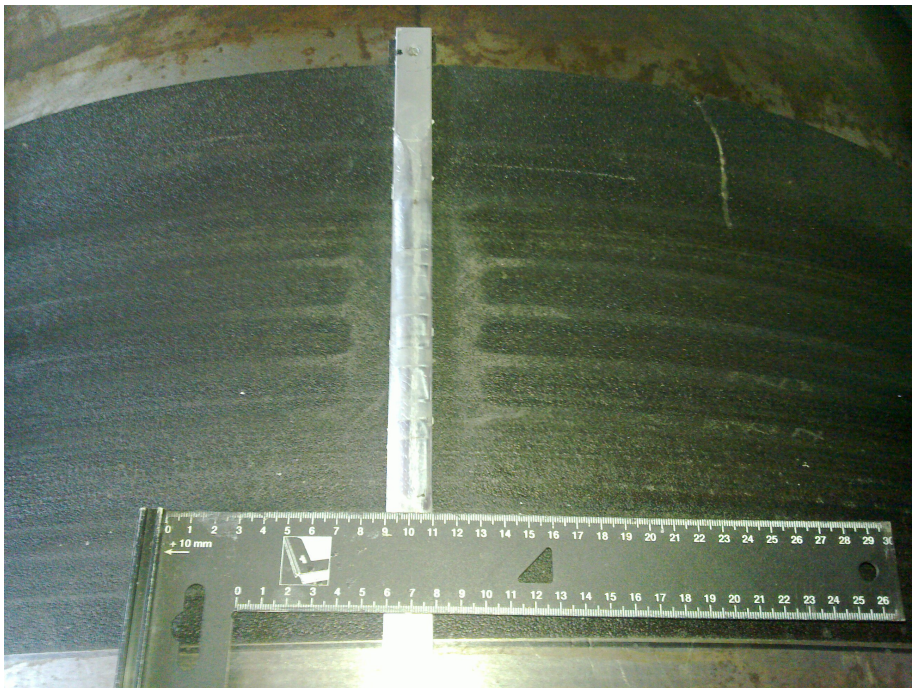

Figure 20: The cleat used for exciting the tyre. The image shows the tread marks made by the tyre to the cleat and to the drum. The tread marks show the area of no contact by the tyre.

test bench during cleat impact. Some double sided tape was used under the cleat to keep the center of the cleat better attached to the drum surface. The image taken after the tests shows the area of contact of the tyre tread pattern. It can be seen that the cleat has an an area of no tyre ground contact approximately 2 cm wide on both sides.

4.2 Combining Multiple Measurements

To calculate the modal parameters of a tyre using a single accelerometer, multiple measurements have to be made. Combining multiple measurements is easy if the excitation signal is measured, because the timings of the measurements are easy to synchronize. When the excitation is not measured, synchronizing the signals can become more difficult. One solution is to add an additional sensor for detecting the excitation time, but this requires a more complex measurement configuration. Sometimes synchronizing the measurements by using only the measured data might be easier.

In a static tyre the multiple measurements made from the different sides of the tyre at differing times can be synchronized by measuring the time it takes for the vibration impulse to travel around the tyre. This can be done by looking at the measurement from a single point in the tyre, measuring the time difference between multiple passes of the impulse and using equation 21. It is easy to see the impulse travelling around the tyre by using only a single measurement as is shown in figure

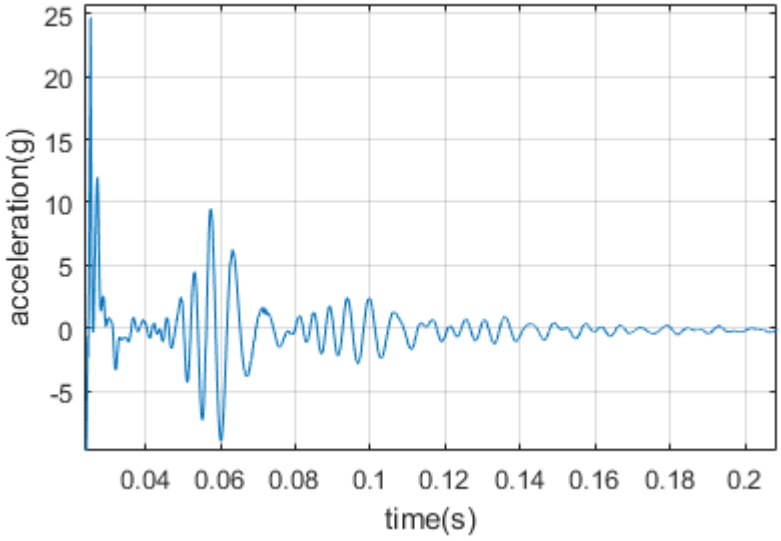

Figure 21: Acceleration measurement of a static tyre from the point of excitation. The impulses travelling around the tyre are clearly visible as vibrations of increased amplitude.

21. Because the highest acceleration value measured in every position corresponds to the same initial peak of the impact, all of the measurements can first be aligned by using the highest value of each measurement. After the measurements have been aligned it is possible to use the distance of the measurement point from the excitation point along the treadband and the group velocity to calculate the time delay between measurements. When the time delay is known, all that is needed for synchronizing the measurements is to shift the maximum aligned measurements with the delay values calculated.

For a rolling tyre without cleat excitation combining multiple measurements is not necessary, because the vibrations of a rotating tyre are almost identical between multiple rotations. In figure 22 scanning measurements from 26 rotations around the tyre are compared by plotting them on top of each other. The slight variations between rotations are small enough to likely fall within measurement inaccuracies and slight variations in speed. This similarity means that a rolling tyre with continuous and unchanging excitation by the contact patch does produce a constant deformation shape. The shape is formed because the excitation doesn't change and therefore the whole interference pattern of all the waves stays constant. This constant deformation shape is not the same thing as a standing wave, because in a standing wave the acceleration is constant only at the nodal points. By measuring the accelerations of this deformation shape it should later be possible to differentiate between the vibration caused by cleat excitation and the vibrations belonging to the deformation shape.

When the tyre is excited by a cleat, the excitation causes vibrations travelling around the deformed tyre. Because the accelerometer measurements is a scanning measurement when viewed from the global coordinates, it is necessary to differentiate

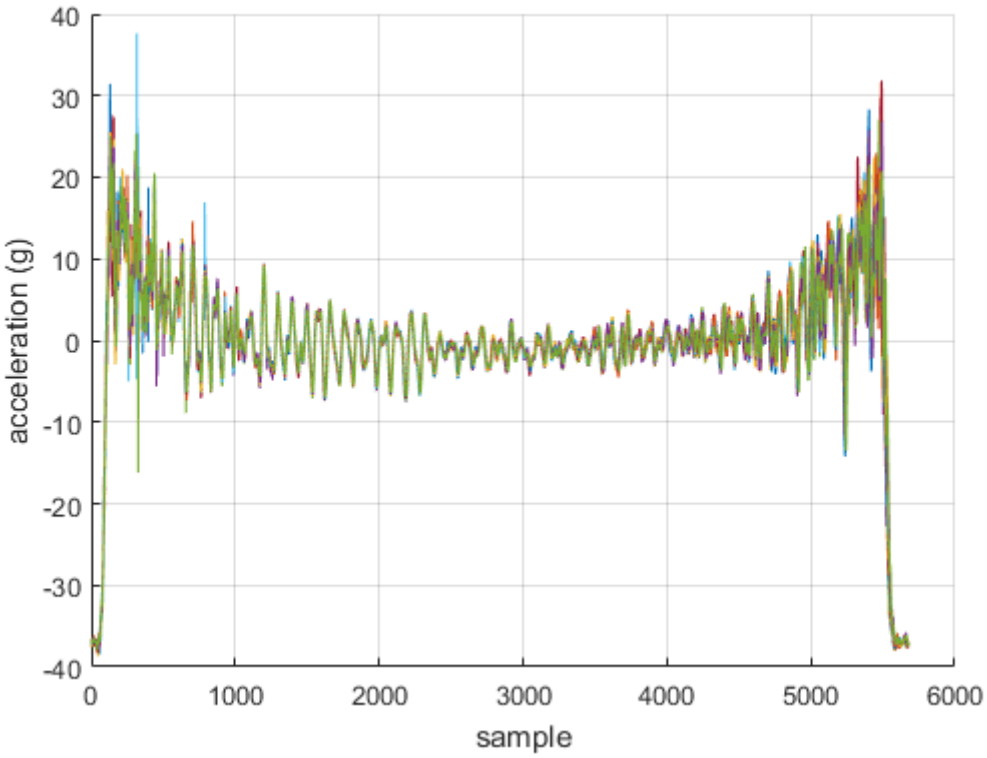

Figure 22: Acceleration measurements of a rolling tyre without cleat excitation for 26 rotations around the tyre. In this figure there are 26 different synchronized scanning measurements plotted on top of each other. The starting points of the measurements along the tyre have been matched to easily compare the differences. The rolling speed was 30 km/h, tyre load 4 kN, inflation pressure 2.2 bar and sampling rate 25.6 kHz.

between acceleration values resulting from the accelerometer moving through the constant deformations of the tyre and the vibrations resulting from the cleat excitation. This can be done by first measuring the acceleration values without the cleat, and then comparing them to the acceleration values measured with the cleat. The vibrations caused by the cleat can then be calculated by subtracting the static deformation acceleration values from the cleat excited values. The subtraction has to be performed so that the acceleration values at the same position around the tyre are compared.

Because we have only a single accelerometer moving with the tyre, it is impossible to measure all of the tyre vibrations from one cleat excitation. To measure all of the modes we should have an accelerometer on every point of the tyre rubber. This means that we will need multiple measurements with the same cleat excitation. Because we are only using a single accelerometer that rotates with the tyre, the sensor will measure vibrations from multiple positions during one cleat excitation event. Additionally, we have to be able to deduce where the accelerometer was when the cleat contacted the tyre, because the time and the point of measurement both

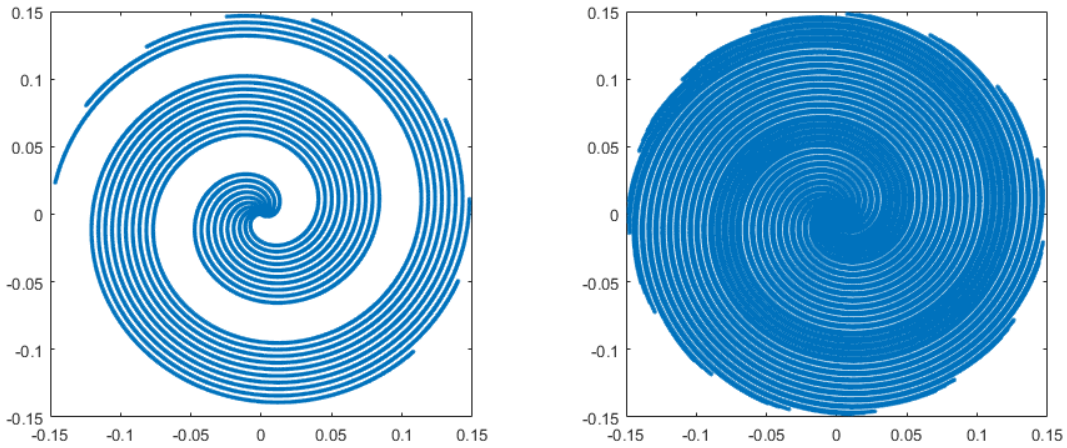

(a) The points recorded after measuring 10 cleat excitations.

(b) The points recorded after measuring 50 cleat excitations.

Figure 23: Representation of the collected samples in the space formed by angle and time from cleat excitation. Each sample is plotted as a point in the polar coordinates. The angle of the point corresponds to the angle of the accelerometer and the distance from the origo corresponds to the time passed from the initial contact between the cleat and the tyre.

change during the excitation event. The position of the accelerometer at the impact time affects the positions and times we measured. The first method requires an additional sensor, and the second method requires a measurement of the group speed of the travelling impulse. Because the propagation speed of the wave depends on the rotation velocity of the tyre, a hall sensor and a magnet were used to detect the cleat in this experiment.

After we know the position of the accelerometer at the moment of excitation, it is possible to combine multiple measurements to record the complete response of the tyre to the cleat excitation. If the radii of the tyre and drum don't change during the experiment and there is no slippage, the space formed by the sensor angle and time from excitation is filled in a way that depends only on the ratio between the tyre circumference and the drum circumference. When the number of cleat excitations is increased, the time resolution for the combined measurement of a fixed sensor angle also increases. However, the resolution doesn't increase uniformly, which means that the number of measurement made has to be considered carefully. For these measurements, a short MATLAB script was created to show how the measurements made from multiple excitations populate the angle-time space. For drum and tyre diameters of 1.219 m and 0.59 m respectively, the samples filling the angle-time space have been visualised in figure 23.

When we know the arrival times of the cleat under the tyre, it is possible to create a new time variable for the combined measurements by always resetting it to zero when the cleat arrives under the tyre and increasing it by the sampling interval for every measurement after that. After we have added this new time value to every

measurement, we can divide the tyre into small sections, group the measurements into those sections by using the encoder angle and then sort the measurements of the same section based on the newly created time from cleat excitation. Measurements with the same time value inside the segment can be averaged to reduce random error. After all of this we have a complete excitation measurement from every point of the tyre for the selected cleat and rolling velocity.

4.3 Static Tyre

The measurement data for the static tyre was analysed by using the SSI method presented in section 2.4 to detect the natural frequencies and mode shapes. To validate the mode shapes and natural frequencies a second analysis method based on the FRFs, and presented on sections 2.2 and 2.3, was also used on the same data.

For the preprocessing of the SSI method the first 0.0127 seconds after the starting point of the hammer impact were removed from the data to have zero input force during identification and to let the modes with frequencies with most damping die out. It was noticed after multiple identification rounds that by removing the first 324 data points, corresponding to 0.0127 seconds worth of data at the sampling frequency of 25600 Hz, the identification algorithm detected the modes more consistently at the frequency range of 0 to 400 Hz.

The multiple excitations on the different portions around the tyre were synchronized using the impact hammer signal as mentioned in section 4.2. It was further recognized that the synchronization detecting multiple passes of the same impulse travelling around the tyre as explained in section 4.2 provided approximately the same synchronization results.

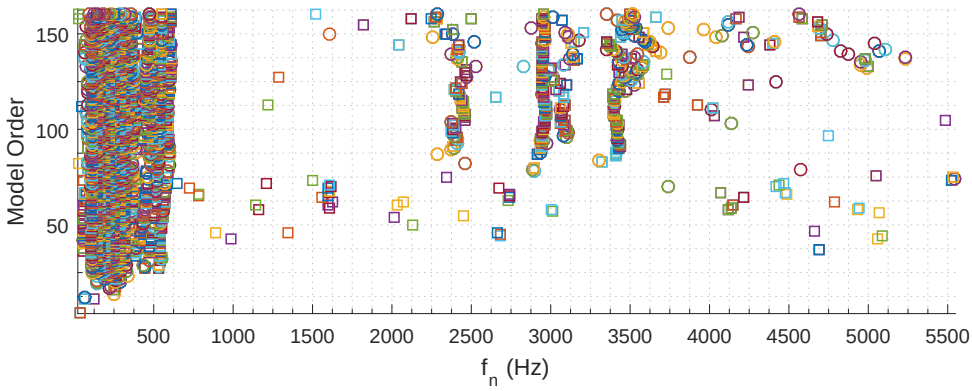

(a) The stabilization diagram zoomed from 0 to 5500 Hz.

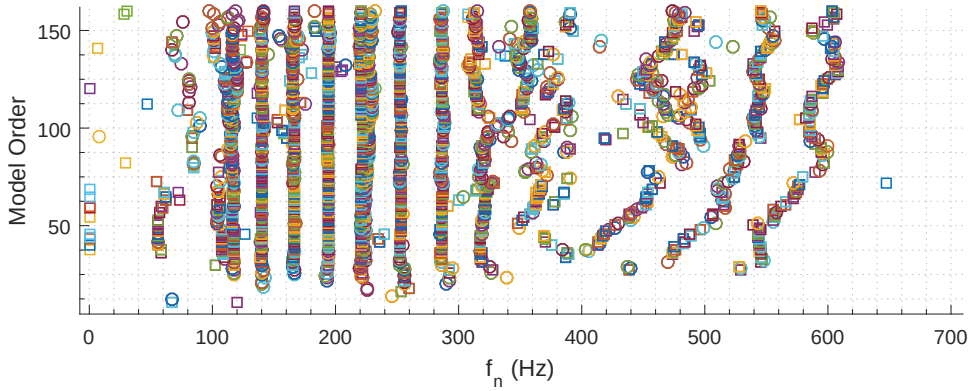

(b) The stabilization diagram zoomed from 0 to 700Hz

Figure 24: The stabilization diagrams of the SSI identification of a static tyre with two different zoom levels. The meaning of the different symbols has been explained in section 2.5

The identification of the modes with the SSI method was performed with state numbers varying from 1 to 160. The stabilization diagrams of these identification results are shown in figure 24. From the figure it is possible to see that some very clear natural frequencies are identified, while some of the identification results remain somewhat ambiguous. The three lines forming in the stabilization diagram at 2450 Hz, 2950 Hz and 3450 Hz are most likely due to the rotational waves travelling in the treadband. These vibrations have a cut-on frequency of around 2500 Hz as explained in section 3.2. These high frequency modes were not visualised nor listed as natural frequencies because the SSI algorithm was not able to detect the mode shapes reliably enough for these frequencies at any model order tested.

From the low frequency vibrations modes (1,0), (9,0) and the first acoustic mode include the highest uncertainties. Especially the detected natural frequency of the (1,0) mode varies significantly depending on the number of modes identified. From these diagrams and by evaluating the clarity of the mode shapes the SSI identification with a state number of 85 was selected. The natural frequencies identified by the 85 mode SSI are presented in table 2. The numbering of the modes uses the methodology presented in section 3.2, where the first number signifies the circumferential and the

Table 2: The detected natural frequencies and mode numbers of the tyre modes with the SSI and FRF methods for the static tyre. The modes not detected were marked with (-), the modes detected only in the radial direction with (R) and the modes detected only in tangential direction with (T).

Mode Number	F_n**(SSI)**	F_n**(FRF)**	**Damping(SSI)**	**Damping(FRF)**
(1,0)	107.0 Hz	105.6 Hz (T)	12.46%	7.57% (T)
(2,0)	116.3 Hz	118.4 Hz	3.04%	4.77%
(3,0)	140.0 Hz	140.8 Hz	2.31%	5.33%
(4,0)	166.3 Hz	166.4 Hz	2.66%	3.46%
(5,0)	193.7 Hz	192.0 Hz	2.51%	4.04%
(6,0)	221.7 Hz	220.8 Hz	2.29%	2.73%
(7,0)	253.4 Hz	252.8 Hz	2.70%	2.97%
(8,0)	286.5 Hz	284.8 Hz	3.06%	2.90%
(9,0)	320.3 Hz	320.0 Hz (R)	3.56%	3.91% (R)
1st acoustic	227.0 Hz	-	0.7%	-

second the cross-sectional mode shape.

The listed natural frequencies and mode shapes are all detected twice by the SSI algorithm, because the vibrations travelling to opposite directions are detected separately. The mode shapes are complex valued because they describe rotating vibrations. These travelling mode shapes $v = a_v + b_v i$ were then converted to real valued mode shapes v_r that can be visualised using the formula $v_r = sign(b_v)|v|$. Because the phase is forced to become either 1 or -1 the travelling mode shape ends up resembling the standing wave formed by it. The mode shapes detected from the FRFs are shown in figure 25. The mode shapes detected by the 85 mode SSI identification algorithm are visualised in figure 26. The travelling modes of the tyre are visualised as a standing wave consisting of two travelling modes for each frequency visualised. The first acoustic mode of the tyre was detected only when using the SSI method.

4.4 Static Tyre With Ground Contact

For these measurements the tyre was pressed against the ground by a hydraulic cylinder using 4 kN of force. The tyre was excited from the highest point of the tyre and rotated 20 degrees after each trial to relocate the embedded accelerometer. The data was again synchronized using the input force measurements and analysed by using the SSI and FRF methods. For the SSI method 324 data points were removed from the beginning of the measurement data starting from the first contact of the impact hammer. This corresponds to the same 0.0127 s of measurement data

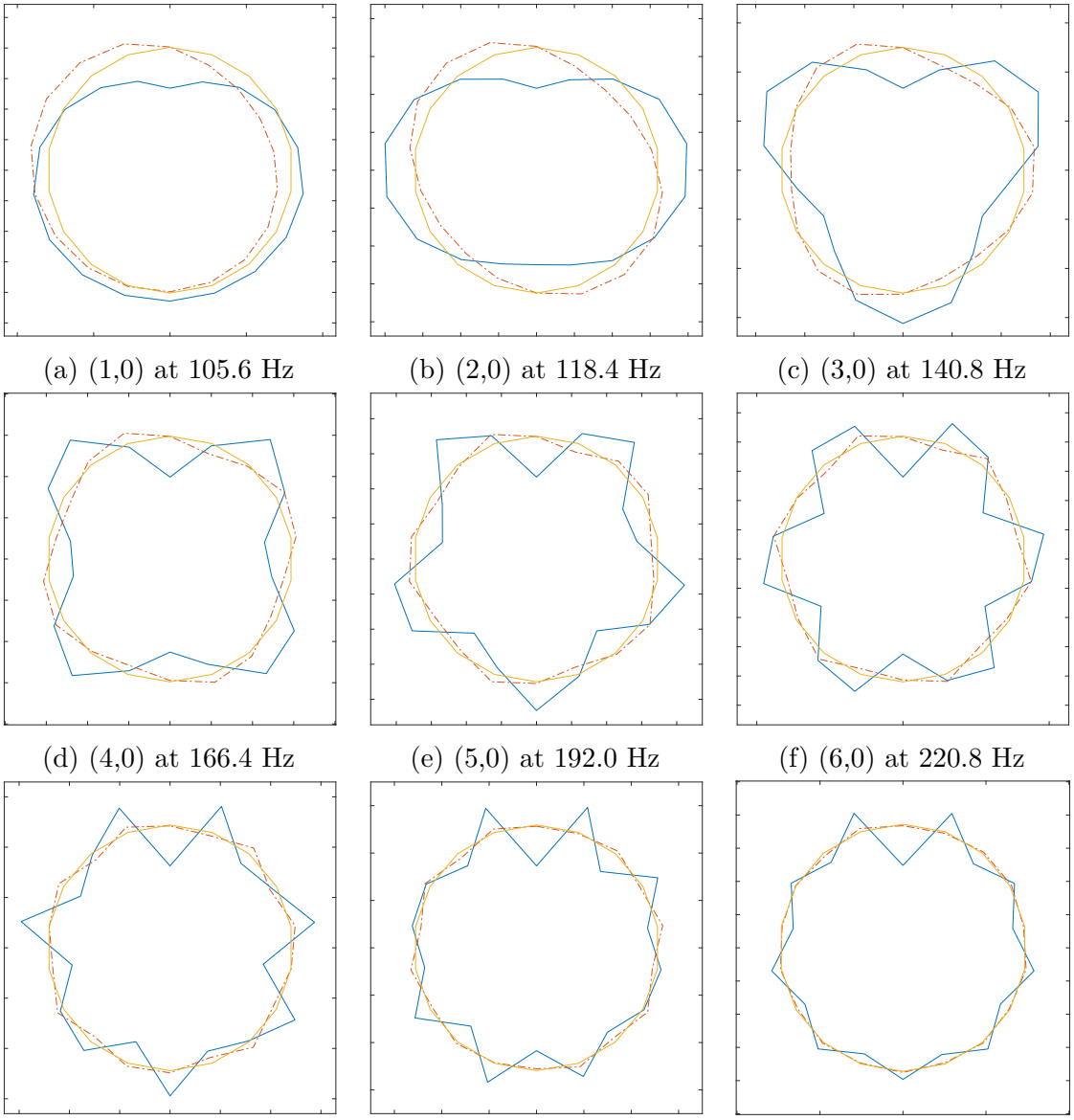

(a) (1,0) at 105.6 Hz (b) (2,0) at 118.4 Hz (c) (3,0) at 140.8 Hz

(d) (4,0) at 166.4 Hz (e) (5,0) at 192.0 Hz (f) (6,0) at 220.8 Hz

(g) (7,0) at 252.8 Hz (h) (8,0) at 284.8 Hz (i) (9,0) at 320.0 Hz

Figure 25: The mode shapes detected using the FRF algorithm from the static tyre. The blue solid line represents the radial component of the mode shape and the red dotted line represents the tangential component. The magnitude of a point is represented as a radial distance from the yellow circle. All shapes have been scaled to approximately even amplitude.

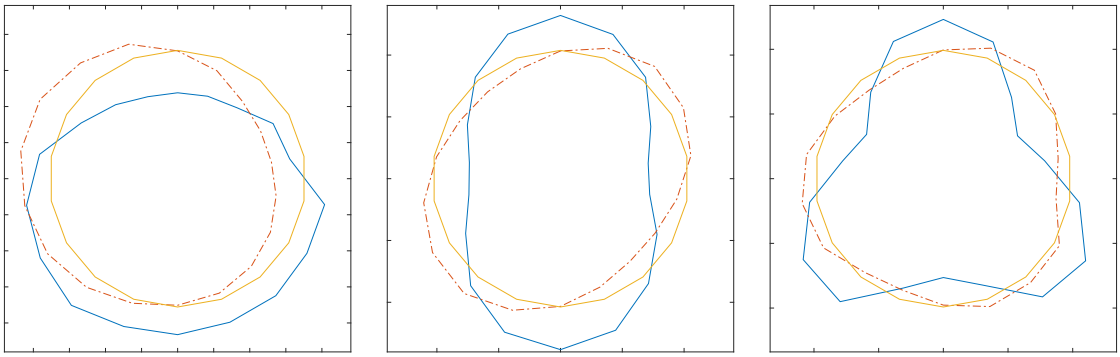

(a) (1,0) at 107.0 Hz

(b) (2,0) at 116.3 Hz

(c) (3,0) at 140.0 Hz

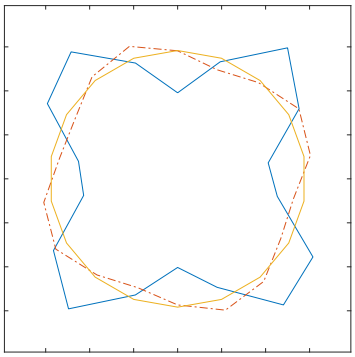

(d) (4,0) at 166.3 Hz

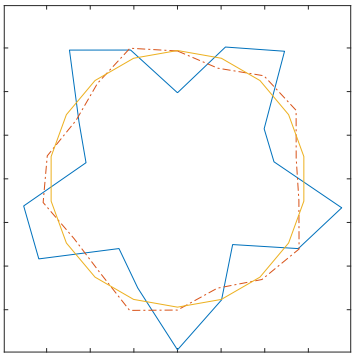

(e) (5,0) at 193.7 Hz

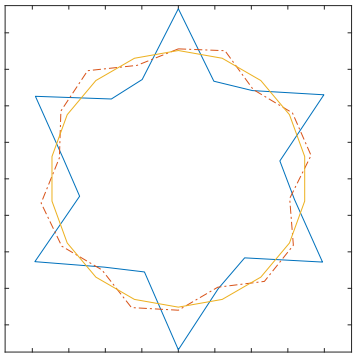

(f) (6,0) at 221.7 Hz

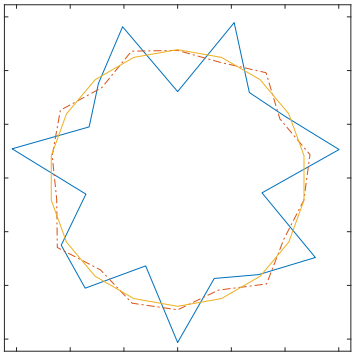

(g) (7,0) at 253.4 Hz

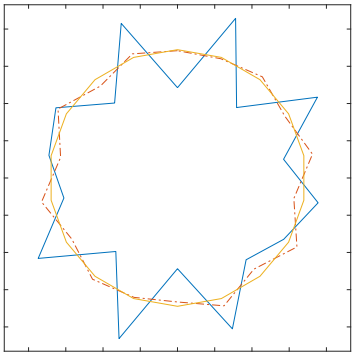

(h) (8,0) at 286.5 Hz

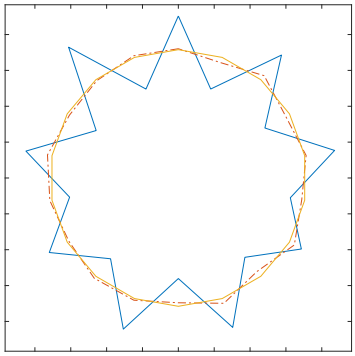

(i) (9,0) at 320.3 Hz

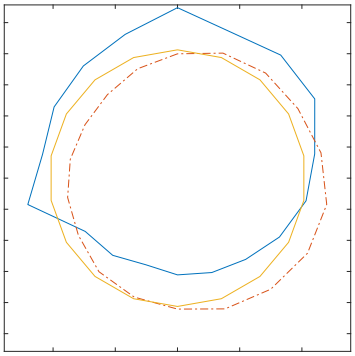

(j) 1st aco. at 227.0 Hz

Figure 26: The mode shapes detected from the static tyre by using the SSI algorithm with 85 modes visualised as standing waves. The blue solid line represents the radial component of the mode shape and the red dotted line represents the tangential component. The magnitude of a point is represented as a radial distance from the yellow circle. All shapes have been scaled to approximately even amplitude.

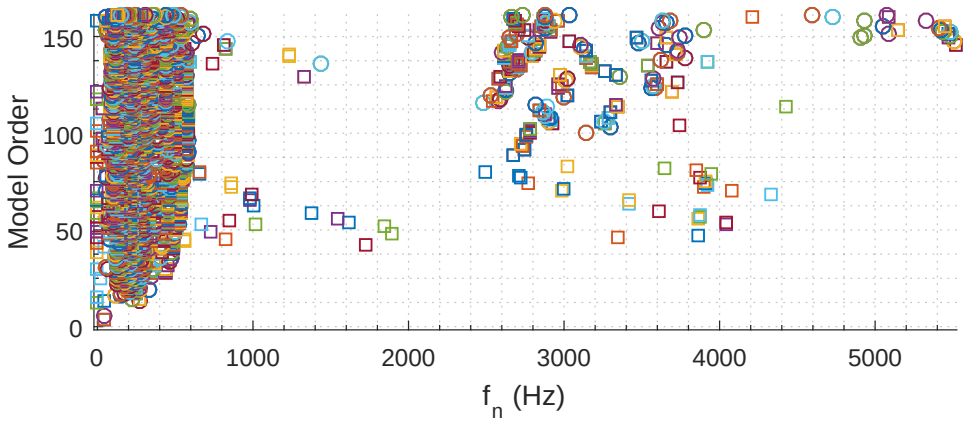

(a) The stabilization diagram zoomed to range of 0 to 5500 Hz.

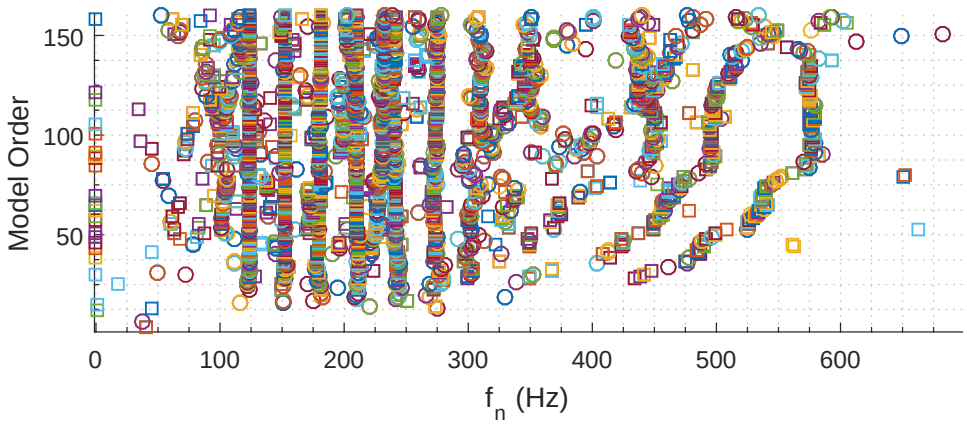

(b) The stabilization diagram zoomed to range 0 to 700Hz

Figure 27: The stabilization diagrams of the SSI identification with two different zoom levels for the static tyre with ground contact. The meaning of the different symbols has been explained in section 2.5

that was also removed from measurements performed without ground contact. The stabilization diagrams plotted for the tyre with ground contact using the SSI method are shown in figure 27.

The natural frequencies of the tyre detected by using the SSI and FRF methods for the static tyre with ground contact are shown in table 3. Only vertical modes and modes with an extremum in the middle of the contact patch were detected using either identification method. In other naming conventions the modes named with the label **extr.** are often differentiated by using a circumferential mode number that is one half higher than the one listed here. Further explanation on the naming conventions used can be found from section 3.2.

The mode shapes detected by the FRF and SSI identification methods are shown in figures 28 and 29 respectively. This time it is possible to see how the ground contact forces the shape to become zero in the middle of the contact patch. It should be noted that all of the detected mode shapes were left-right symmetric. This may be caused by the symmetric position of the excitation point at the top of the tyre. The

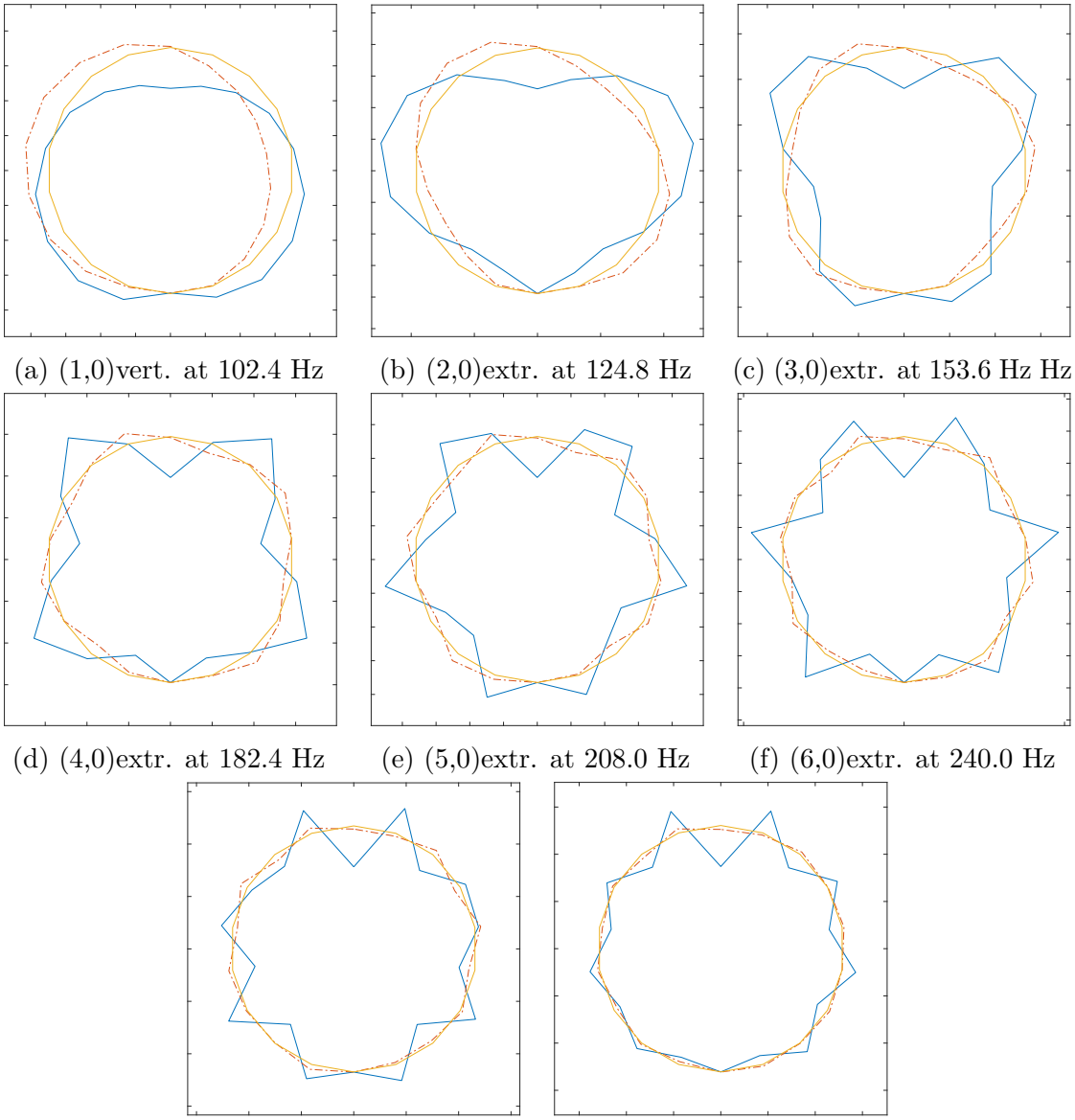

(a) (1,0)vert. at 102.4 Hz (b) (2,0)extr. at 124.8 Hz (c) (3,0)extr. at 153.6 Hz Hz

(d) (4,0)extr. at 182.4 Hz (e) (5,0)extr. at 208.0 Hz (f) (6,0)extr. at 240.0 Hz

(g) (7,0)extr at 275.2 Hz (h) (8,0)extr. at 307.0 Hz

Figure 28: The mode shapes detected using the FRF based algorithm from the static tyre with ground contact. The blue solid line represents the radial component of the mode shape and the red dotted line represents the tangential component. The magnitude of a point is represented as a radial distance from the yellow circle. All shapes have been scaled to approximately even amplitude.

Table 3: The natural frequencies and mode numbers detected from the static tyre with ground contact using the SSI and FRF methods. The undetected modes were marked with (-), the modes detected only in the radial direction with (R) and the modes detected only in the tangential direction with (T).

Mode Number	F_n**(SSI)**	F_n**(FRF)**	**Damping(SSI)**	**Damping(FRF)**
(1,0)vert.	97.7 Hz	102.4 Hz	20.2%	18.6%
(2,0)extr.	123.0 Hz	124.8 Hz	3.92%	6.01%
(3,0)extr.	153.0 Hz	153.6 Hz	2.94%	4.39%
(4,0)extr.	179.8 Hz	182.4 Hz	2.17%	4.00%
(5,0)extr.	210.0 Hz	208.0 Hz	2.24%	3.68%
(6,0)extr.	242.4 Hz	240.0 Hz	2.15%	3.46%
(7,0)extr.	270.8 Hz	275.2 Hz	1.46%	3.20%
(8,0)extr.	295.0 Hz	307.0 Hz	1.78%	6.32%
1st acoustic vert.	230.7 Hz	230.4 Hz	2.14%	3.69%

first acoustic mode was found by using both identification methods, but the shape produced by the FRF method for the mode was nearly identical to the shape of the (6,0)extr. mode. Therefore, the shape of the first acoustic mode was not separately visualised. Another interpretation of this is that the shape of the first acoustic mode was not really identified by the FRF method.

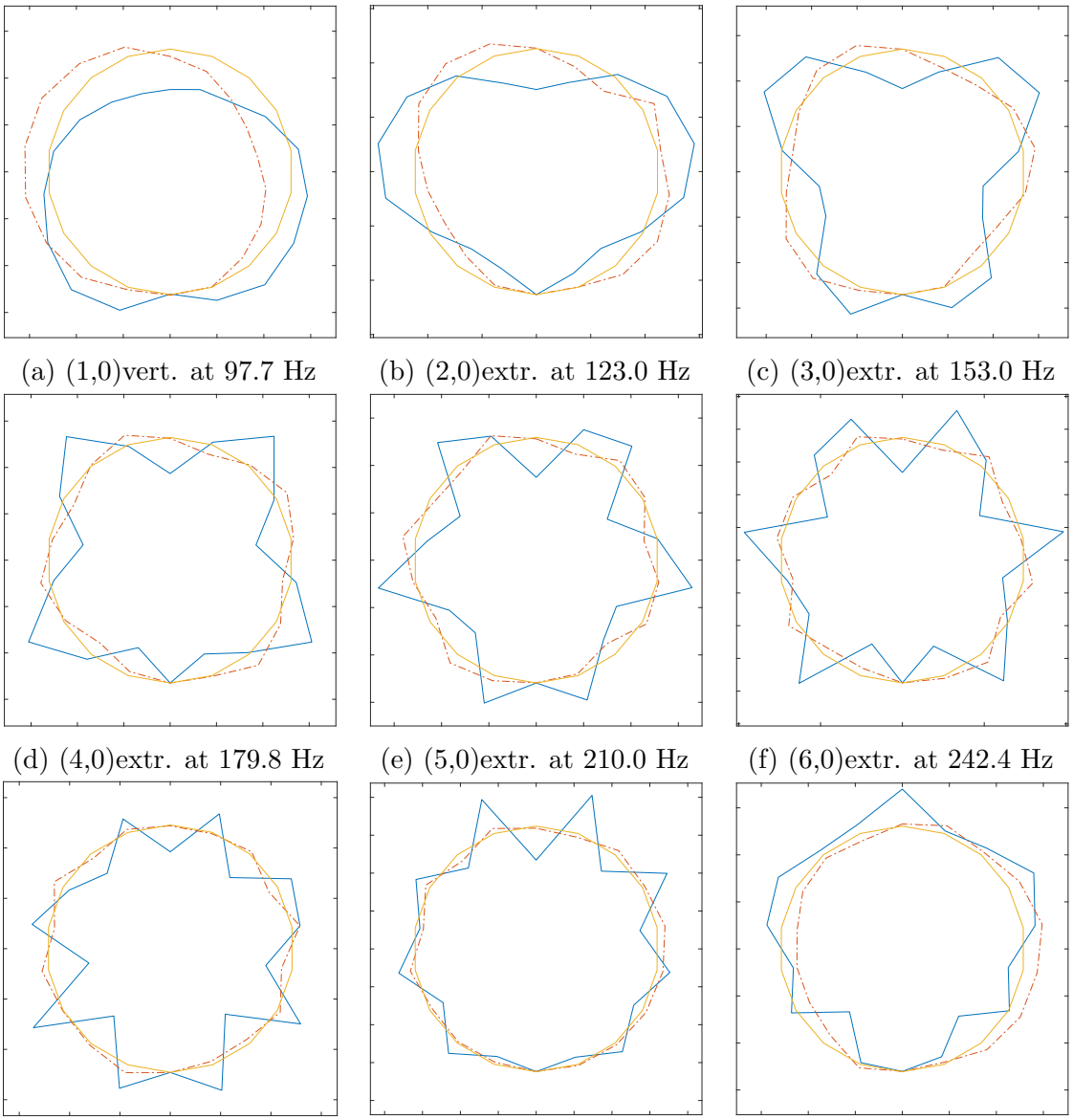

(a) (1,0)vert. at 97.7 Hz (b) (2,0)extr. at 123.0 Hz (c) (3,0)extr. at 153.0 Hz

(d) (4,0)extr. at 179.8 Hz (e) (5,0)extr. at 210.0 Hz (f) (6,0)extr. at 242.4 Hz

(g) (7,0)extr at 270.8 Hz (h) (8,0)extr. at 295.0 Hz (i) 1st aco. vert. at 230.7 Hz

Figure 29: The mode shapes detected form the static tyre with ground contact using the SSI algorithm with 85 modes visualised as standing waves. The blue solid line represents the radial component of the mode shape and the red dotted line represents the tangential component. The magnitude of a point is represented as a radial distance from the yellow circle. All shapes have been scaled to approximately even amplitude.

4.5 Rolling Tyre

In these measurements the vibrations of a rolling tyre were measured while rolling on a smooth drum. The accelerometer rotating with the tyre can provide a very high position resolution because of the high sampling rate. The down side is that it is possible to get measurements from the same position only once per rotation. In the case of a smooth drum or flat road this doesn't matter, because multiple rotations of the tyre always produce the same acceleration values at the same measurement position as was earlier shown in section 4.2 and figure 22. This makes it very difficult if not impossible to detect the modes of the tyre with a measurement of this kind. In this thesis these measurements are used to evaluate the performance of the flexible ring model presented in section 2.6 and to remove the accelerations caused by the static deformation pattern in the measurements with cleat excitation.

The measurements were made with a 4 kN load on the tyre and a 2.2 bar tyre air pressure and a sampling rate was 25600 Hz. The high frequency of measurement allows digital filtering of the signal quite easily. It should also ensure that most frequencies present in the tyre are seen in the measurements.

The results of these measurements can be seen in figure 30. The Earth's gravitational field causes a sine wave like pattern that is clearly visible at low velocities. It is possible to see that the amplitudes of the vibrations increase everywhere on the tyre with increasing rotation speed. It is also possible to see the damping effect of the tyre rubber on the vibration as a decrease in amplitude when moving further away form the contact area.

For the radial acceleration measurements there is a single large negative peak signifying the disappearance of the centripetal force. This is caused by the linear path of the accelerometer when it follows the ground surface with the rubber. The centripetal acceleration of the rotating motion is only observed once it disappears because the sensor acts as a high pass filter as was explained in section 4. In the tangential acceleration measurements the edges of the ground contact area can be seen as a high positive and a high negative peak. These peaks are caused by the sudden compression and expansion of the rubber as it enters and leaves the contact area.

The measured accelerations are not completely radial or axial at the contact patch because the sensor gets aligned with the road as the rubber bends. This results in a constant measured radial acceleration within the contact area, while the true radial acceleration should have a more parabolic shape.

The sine wave caused by the gravitational field could be filtered out with a high pass filter or by removing a sine wave of 1 g amplitude with the correct phase from the measurement. Additionally, the centripetal acceleration could be added back to the measurements by detecting the magnitude of the negative peak and adding it to all measured values. However, this wasn't done for figure 30 to instead show the actual data measured by the sensor as a function of the sensor position.

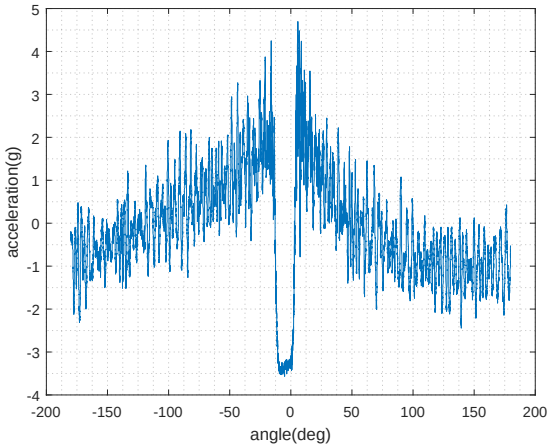

(a) Radial acceleration at 10 km/h.

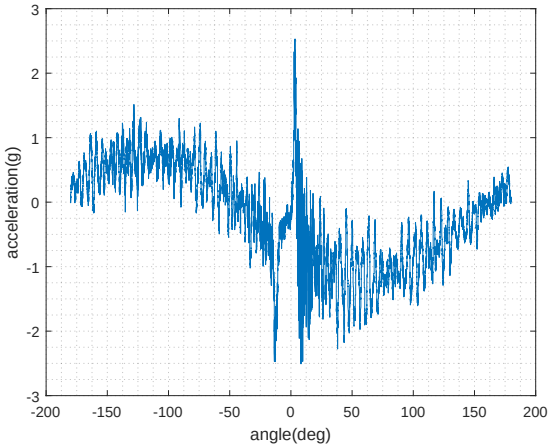

(b) Tangential acceleration at 10 km/h.

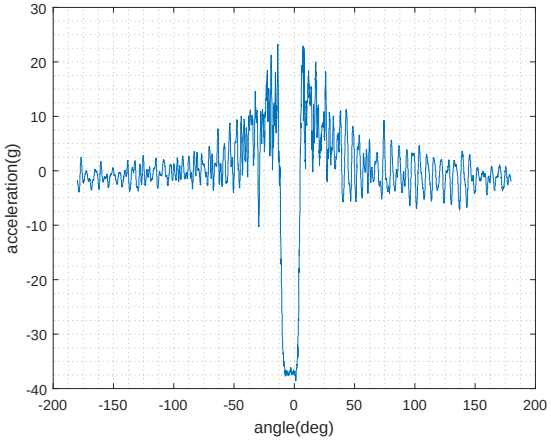

(c) Radial acceleration at 30 km/h.

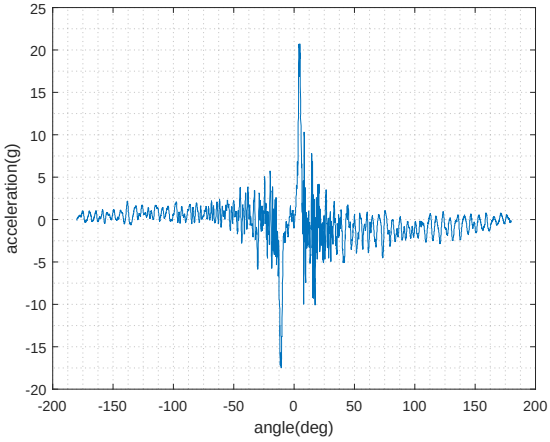

(d) Tangential acceleration at 30 km/h.

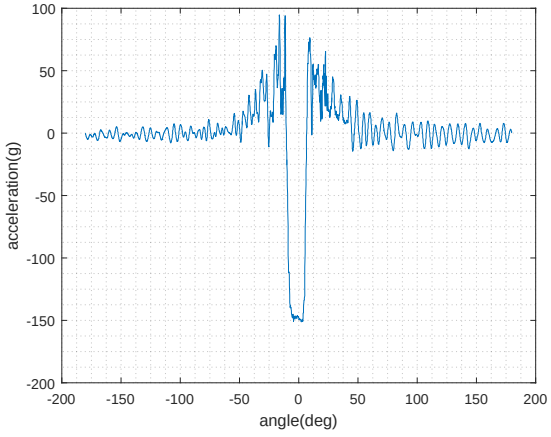

(e) Radial acceleration at 50 km/h.

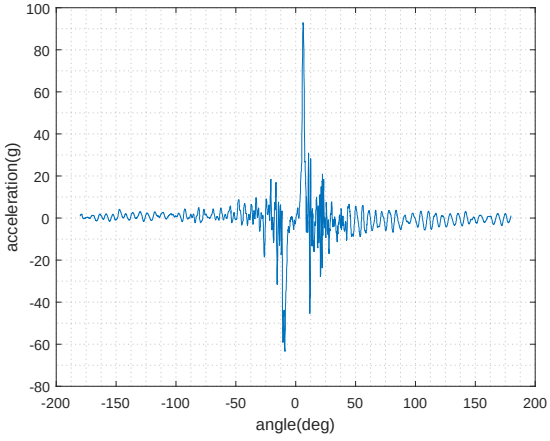

(f) Tangential acceleration at 50 km/h.

Figure 30: The measured acceleration values from a rolling tyre on a smooth drum at different rotation speeds plotted as the function of the sensor angle.

4.6 Rolling Tyre With Cleat Excitation

The measurement results combined from multiple tyre excitations were used as the input for the SSI algorithm. Additionally video visualizations of the accelerations of the tyre during cleat impact were created from all of the three measurements. The tyre was measured at 20, 40, and 60 km/h and the different results are divided under separate sections. For the SSI identification some measurements from the beginning of the data had to be removed to remove the cleat contact from the data and have the input force to the tyre road system be zero. A load of 4 kN was applied to the tyre with the test bench through a suspension system.

The SSI was performed with the number of states going from 1 to 280 to better differentiate the natural frequencies resulting from structural features from mathematical poles. To reduce the computational cost, only 128 of the full 512 points at the tyre circumference were used for the identification. This should still be enough to find all structural modes of the tyre. The poles with low repeatability in the stabilization diagram with different state pole counts often had damping values nearing 100%. These states can be seen in the stabilization diagrams, but they were not considered true natural frequencies of the tyre road system and are therefore not included in the tables containing the natural frequencies.

In all of the mode shape figures presented in this section the tyre is rolling towards the left. This means that the rotation direction is anticlockwise and the left side of the tyre is the front edge.

4.6.1 Tyre rolling at 20 km/h

In this experiment the drum was set to rotate at a constant velocity of 20 km/h and the tyre was driven on the drum for 30 minutes. This provided enough measurement points do divide the tyre to 512 evenly sized sections with a sample rate of 25600 Hz. The cleat impacted the tyre approximately once in two rotations of the tyre, which should give the vibrations time to disappear before new excitation. The cleat caused some visible movement of the suspension system, but the accelerometer attached to the wheel hub showed that the acceleration of the hub was insignificantly small when compared to the values of the accelerations measured at the tyre.

The stabilization diagram comprised of the SSI identification results can be seen in figure 31. Some repeatedly identified natural frequencies can be seen in the diagram but it does seem to contain more mathematical poles than the diagrams of a static tyre. One reason for this may be that the modes of the tyre are more difficult to detect once the rotation of the tyre breaks the symmetry of the physical phenomena affecting the waves travelling in opposite directions. Another reason may be that only two tyre rotations of data with measurements all around the tyre are available for the SSI algorithm. With the static tyre the amount of measurement points is much smaller, but there are measurements from a much longer period of time available for the algorithm.

The natural frequencies and dampings of the consistently identified modes are presented in table 4. Modes (1,0)hort., (2,0)extr., and (5.0)extr. have a high damping but were still identified consistently. All of the theoretically existing modes of the

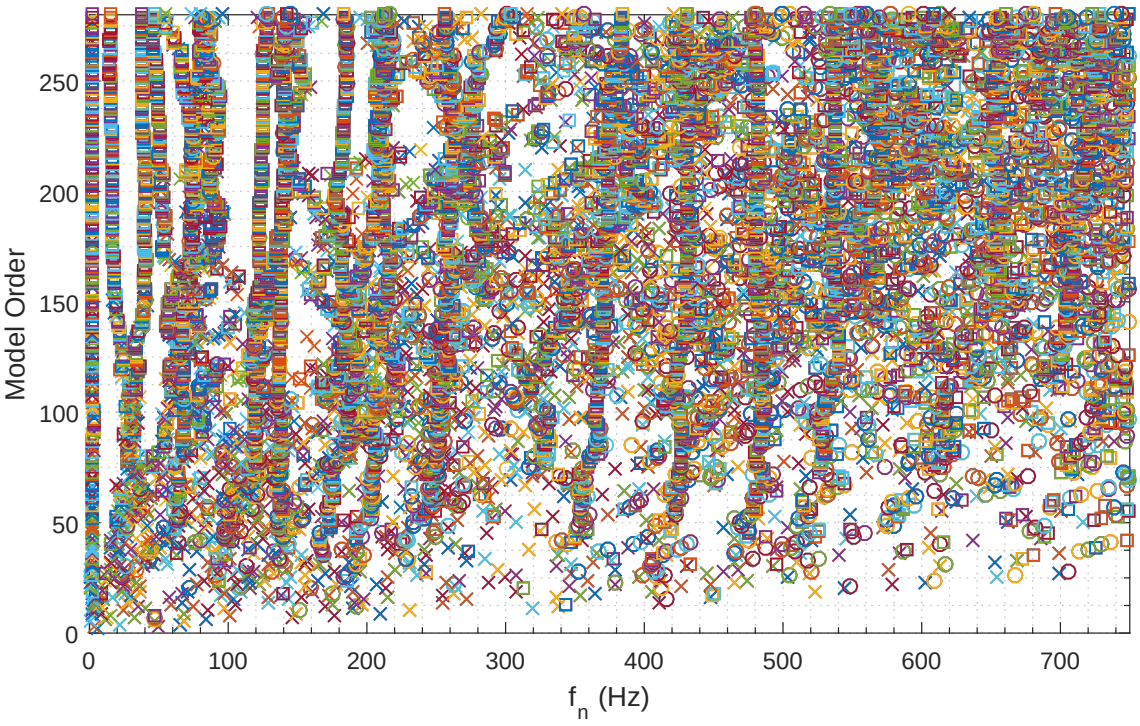

Figure 31: The stabilization diagram of a cleat experiment with 20 km/h rolling speed zoomed to a range between 0 and 750 Hz.

tyre rubber were not detected as in theory there should be a extr. and hort. version of all the mode number pairs. This may be due to insufficient excitation by the cleat for these modes or a very high damping value making them difficult to detect. Additionally, mode (4,0)0 has a higher natural frequency than the mode (5,0)extr. despite the lower circumferential mode number. This is most likely due to the difference between modes with an extremum and modes with a zero at the ground contact patch. Determining the mode shape was very difficult for some of the modes detected, because the complex valued mode shapes have been converted to real valued ones for visually determining the mode shape. This conversion seems to be much more problematic once the symmetry between waves travelling in opposing directions is broken.

The shapes of the modes are shown in figure 32. The modes are now much higher resolution than in the experiments preformed with a non-rotating tyre, but the conversion from complex to real mode shapes doesn't seem to work as well. The conversion is the most likely cause of the sharp edges in many of the shapes. A proper visualization of the modes would require an animation of the mode shapes travelling in both directions. The difficulties of realizing the mode shapes of complex modes was discussed by Imgerun and Ewins in 1993 [34]. All of the modes presented in figure 32 are comprised of two travelling mode shapes combined to visualize them as a standing wave.

For many of the modes in figure 32 it is possible to see some differences in the mode shape magnitudes between the front and back sides of the tyre. One reason

Table 4: The natural frequencies of a tyre rolling 20 km/h identified by using the SSI method.

Mode shape	**Natural Frequency**	**Damping**
(1,0)hort.	74.7 Hz	47.8 %
(2,0)extr.	95.7 Hz	49.3 %
(3,0)0	122.7 Hz	15.7 %
(5,0)extr.	134.4 Hz	56.4 %
(4,0)0	139.0 Hz	11.0 %
(6,0)extr.	181.9 Hz	14.6 %
(7,0)extr.	209.2 Hz	9.8 %
(8,0)0	258.6 Hz	10.3 %
(12,0)extr.	431.1 Hz	4.5 %
(14,0)extr.	479.9 Hz	7.0 %

for the magnitude may be that mode is excited more on the front or rear edge of the tyre and another may be that it is easier for the wave to travel one way around the tyre. The difference in group velocity is also clearly visible in the animations made of the tyre accelerations.

In the measurements made at 20 km/h many of the higher frequency modes were not detected. This may be due to insufficient excitation at some of these higher frequencies. At 20 km/h the cleat moves under the tyre much slower than at the other tested rotation speeds. Once the rolling speed is increased the magnitude of peak force during excitation should increase and the frequency band of the input move up.

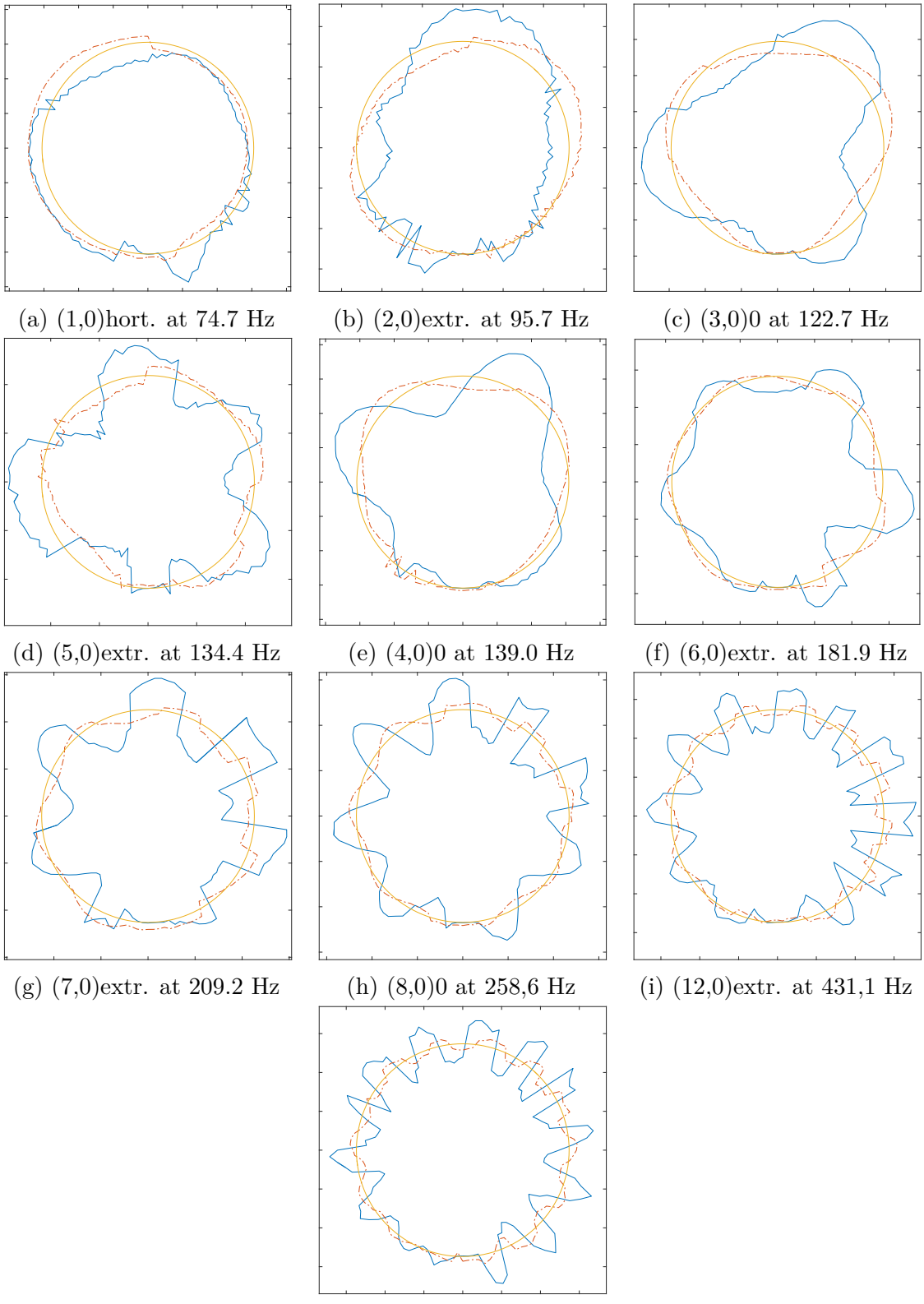

(a) (1,0)hort. at 74.7 Hz (b) (2,0)extr. at 95.7 Hz (c) (3,0)0 at 122.7 Hz

(d) (5,0)extr. at 134.4 Hz (e) (4,0)0 at 139.0 Hz (f) (6,0)extr. at 181.9 Hz

(g) (7,0)extr. at 209.2 Hz (h) (8,0)0 at 258,6 Hz (i) (12,0)extr. at 431,1 Hz

(j) (14,0)extr. at 479.9 Hz

Figure 32: The mode shapes of a tyre rolling 20 km/h with a 4 kN load.

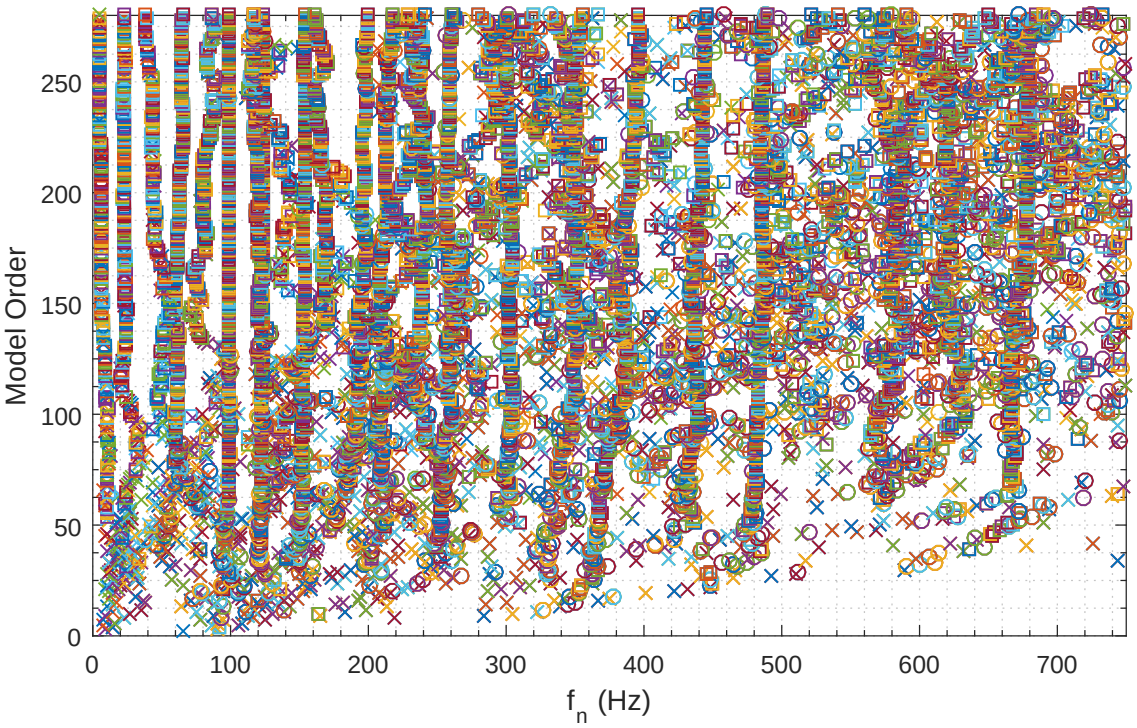

Figure 33: The stabilization diagram of a cleat experiment with 40 km/h rolling speed.

4.6.2 Tyre rolling at 40 km/h

The tyre tests at 40 km/h provided a clearer stabilization diagram than the measurements at 20 km/h as can be seen from figure 33. This should indicate a better identification result. A likely cause is the faster and more powerful excitation by the cleat with this higher rolling speed.

From table 5 it is possible to see that more modes were identified than with the 20 km/h rolling tyre. Especially the modes with a circumferential mode number from 9 to 11 are presented here, while they were missing from the 20 km/h results. Additionally, most of the modes have quite a low damping. The modes with significantly higher damping values than the others are (3,0)extr. and (3,1)extr.. The cross sectional mode number of 2 was assigned to mode (3,2)extr. mainly because it had a higher natural frequency, its mode shape was slightly wavy and the modes with cross-sectional mode shape of 1 should not be visible with an accelerometer in the middle of the tyre. It should also not be possible to have two modes with completely identical mode numbers. However, as there is no way to clearly determine the cross-sectional wave number from these measurements, all of the values for it are mostly based on the low likelihood of detecting modes with high cross-sectional number and the low probability of detecting modes with a cross-sectional mode number of 1.

The mode shapes of the tyre rolling at 40 km/h are presented in figure 34. Some of the modes have acute corners and significant differences between the left and right side of the tyre. This was also the case with the measurements performed at 20 km/h rolling speed. With modes (6,0)extr. and (7,0)extr. there seems to be a significant

Table 5: The natural frequencies of a tyre rolling 40 km/h identified by using the SSI method.

Mode shape	**Natural Frequency**	**Damping**
(2,0)extr.	99.0 Hz	11.1 %
(3,0)extr.	119.0 Hz	39.7 %
(3,0)0	123.0 Hz	7.1 %
(5,0)0	153.2 Hz	4.8 %
(3,2)extr.	169.6 Hz	31.3 %
(6,0)extr.	198.1 Hz	10.5 %
(7,0)extr.	218.1 Hz	8.5 %
(8,0)extr.	241.0 Hz	11.8 %
(9,0)extr.	258.4 Hz	8.8 %
(10,0)extr.	303.0 Hz	9.4 %
(11,0)extr.	353.1 Hz	8.9 %
(10,0)0	396.5 Hz	6.5 %
(13,0)extr.	444.6 Hz	7.0 %
(14,0)extr.	484.9 Hz	6.9 %

reduction of mode amplitude at the point where the forward and backward travelling waves meet. The meeting point is in the left side of the tyre because the rotation of the tyre increases the movement speed of the forward travelling wave and decreases the speed of the opposing wave.

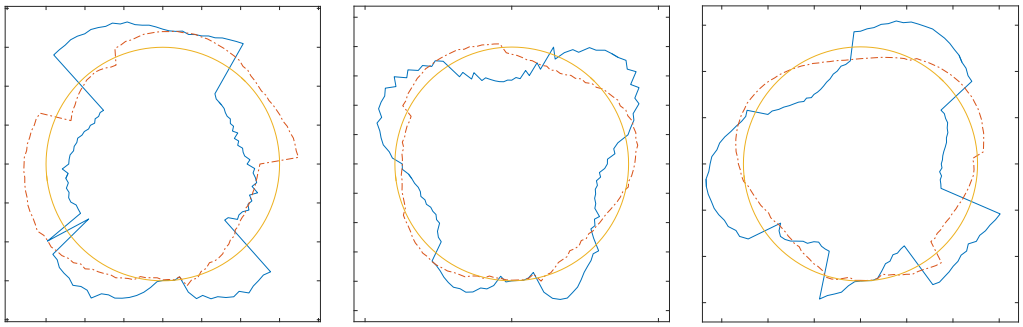

(a) (2,0)extr. at 99 Hz (b) (3,0)extr. at 119 Hz (c) (3,0)0 at 123 Hz

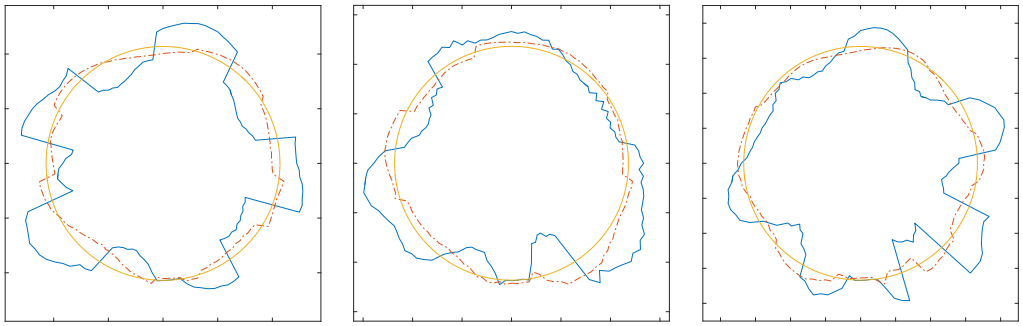

(d) (5,0)0 at 153 Hz (e) (3,2)extr. at 170 Hz (f) (6,0)extr. at 198 Hz

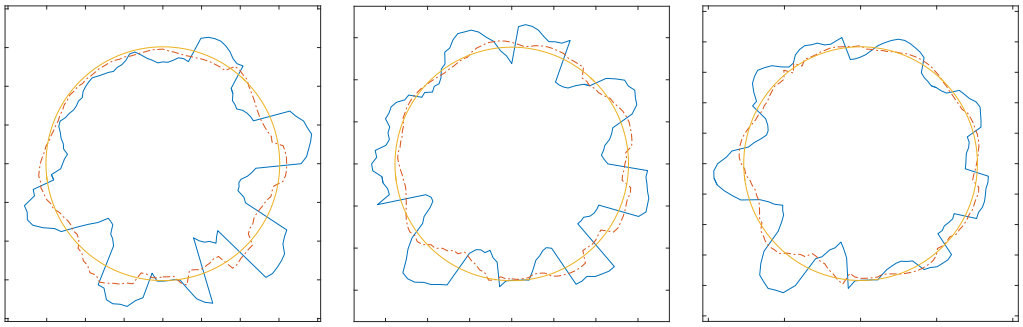

(g) (7,0)extr. at 218 Hz (h) (8,0)extr at 241 Hz (i) (9,0)extr. at 258 Hz

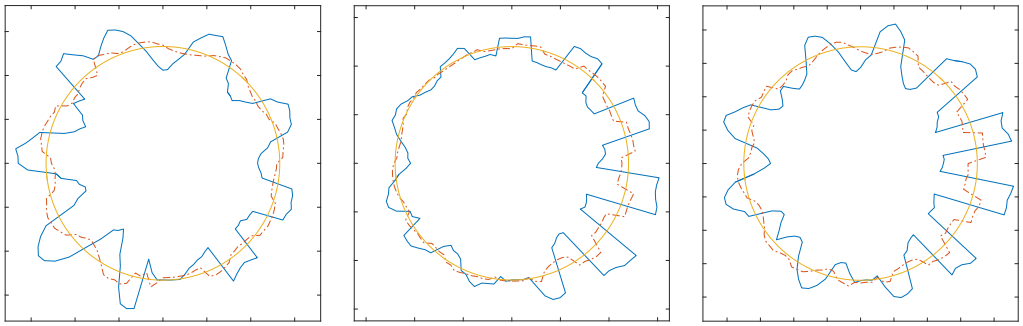

(j) (10,0)extr. at 303 Hz (k) (11,0)extr. at 353 Hz (l) (10,0)0 at 397 Hz

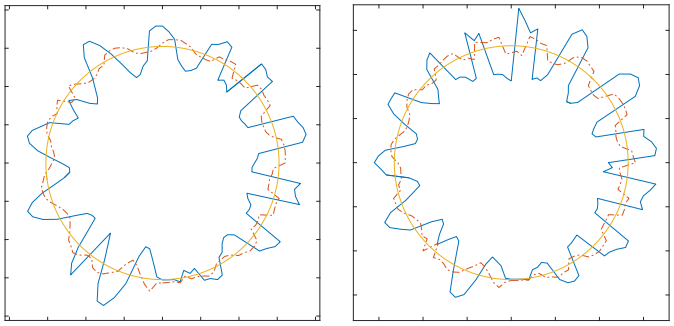

(m) (13,0)extr. at 445 Hz (n) (14,0)extr. at 485 Hz

Figure 34: The mode shapes of a tyre rolling 40 km/h with a 4 kN load.

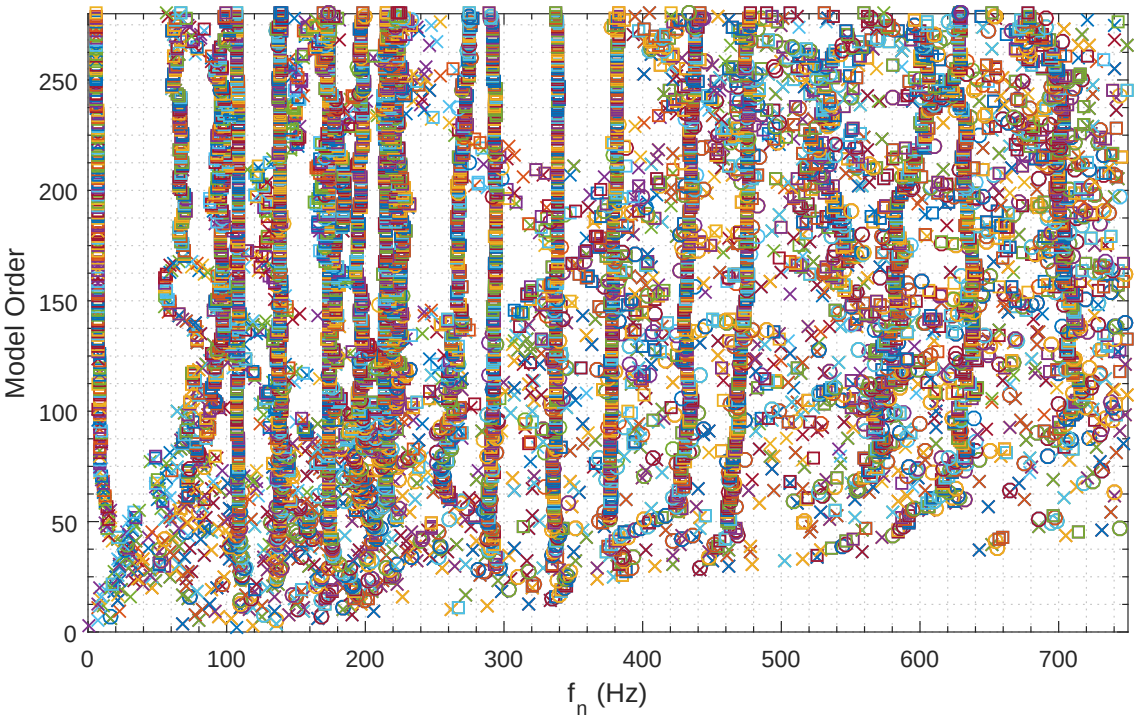

Figure 35: The stabilization diagram of a cleat experiment with 60 km/h rolling speed.

4.6.3 Tyre rolling at 60 km/h

The tyre measurements at a 60 km/h rolling speed produced a stabilization diagram with relatively few numerical modes as is shown in figure 35. There are also very few detected modes with under 100 Hz natural frequency. The most likely reason for this is that the faster excitation and impact results in a frequency spectrum too high to produce vibration at these lower frequencies.

The lowest frequency mode reliably detected was labeled (4,0)extr. and had a natural frequency of 97.3 Hz. The circumferential number of this mode is higher than those of the others near the same frequency. The (4,0)extr. mode has a high damping of 57.8 %. The lowest frequency mode, with a significantly lower damping, was mode (3,0)0 with a 108.4 Hz natural frequency and a damping of 10.7 %. The measurements at 60 km/h rolling speed produced the mode with the highest circumferential mode number at a natural frequency of 475.2 Hz. The modes, their natural frequencies and damping are presented in table 6.

The mode shapes of the tyre rolling at 60 km/h are shown in figure 36. The classification of shapes (4,0)0, (6,0)0 and (8,0)extr. is difficult because some of the peaks are not as clear as in the other measured mode shapes. In addition to missing the modes for circumferential mode numbers of 0, 1 and 2, the modes with a circumferential mode shape of 12 or 13 were not detected reliably.

The mode shapes (14,0)extr. and (15,0)0 seem to be excited better at the front edge of the tyre and possibly travel only against the tyre rotation direction. An indication of this is the steady decrease in amplitude of these mode shapes when

Table 6: The natural frequencies of a tyre rolling 60 km/h identified by using the SSI method.

Mode shape	**Natural Frequency**	**Damping**
(4,0)extr.	97.3 Hz	57.8 %
(3,0)0	108.4 Hz	10.7 %
(5,0)extr.	139.0 Hz	6.1 %
(7,0)extr.	173.6 Hz	4.1 %
(6,0)0	196.5 Hz	15.0 %
(8,0)0	214.4 Hz	6.8 %
(8,0)extr.	224.4 Hz	13.4 %
(9,0)0	273.8 Hz	14.9 %
(10,0)extr.	293.9 Hz	6.5 %
(11,0)0	338.6 Hz	5.5 %
(12,0)extr.	379.7 Hz	6.9 %
(14,0)extr.	433.9 Hz	8.4 %
(15,0)0	475.2 Hz	7.6 %

moving clockwise along the tyre. Visually it was determined from the tyre vibrations animations that a part of a wave arriving at the tyre contact area will get reflected back from the boundary region. It is likely the case that some mode shapes tend to reflect back more than others. A mode shape that always seems to decrease in amplitude in one direction around the tyre may also be a mode that doesn't reflect back very well at the ground contact area.

In the case of the rolling tyre it is also good to keep in mind that the system is not closed in terms of energy, but may instead receive additional excitation and an amplification of certain frequencies at the contact patch. This means that a vibration travelling through the bottom of the tyre may be amplified while going through.

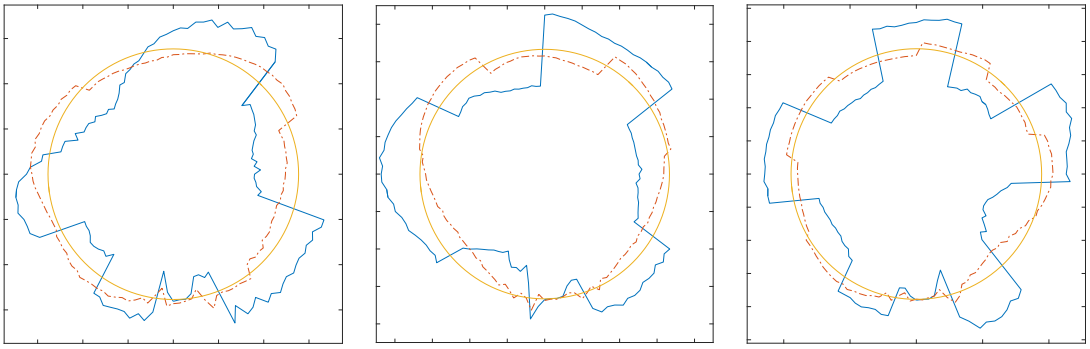

(a) (4,0)0 at 97.3 Hz (b) (3,0)0 at 108.4 Hz (c) (5,0)extr at 139.0 Hz

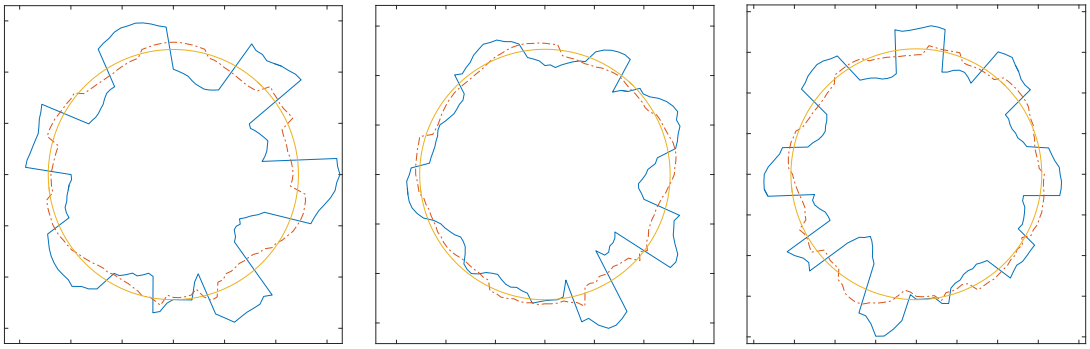

(d) (7,0)extr. at 173.6 Hz (e) (6,0)0 at 196.5 Hz (f) (8,0)0 at 214.4 Hz

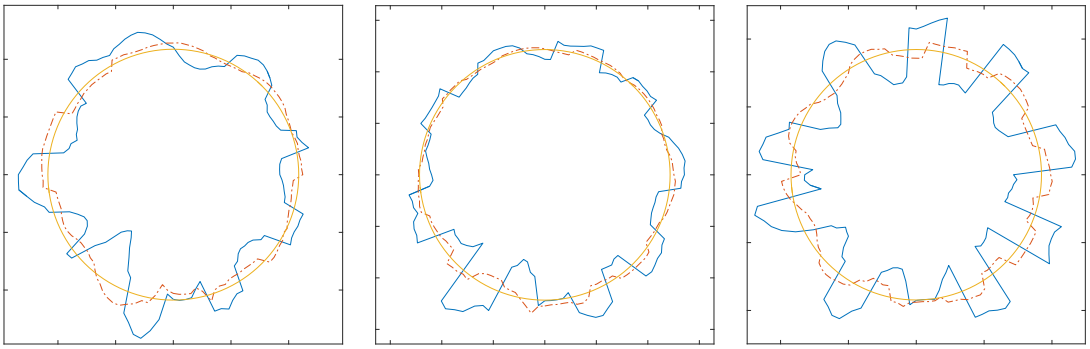

(g) (8,0)extr. at 224.4 Hz (h) (9,0)0 at 273.8 Hz (i) (10,0)extr. at 293.9 Hz

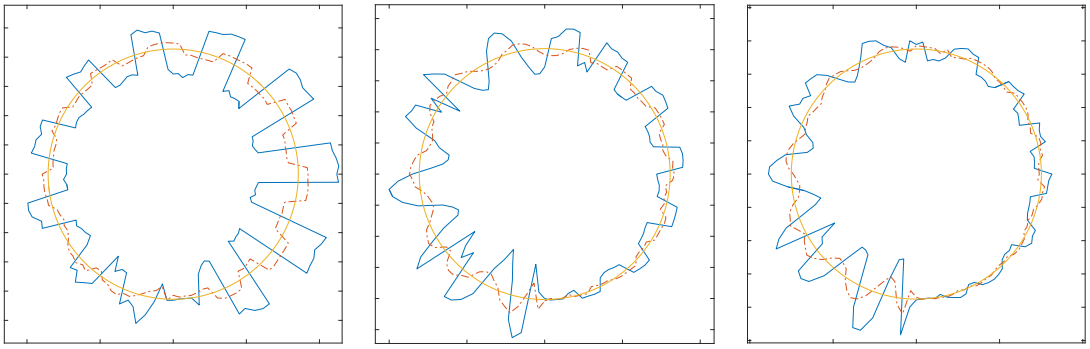

(j) (11,0)0 at 338.6 Hz (k) (14,0)extr. at 433.9 Hz (l) (15,0)0 at 475.2 Hz

Figure 36: The mode shapes of a tyre rolling 60 km/h with a 4 kN load.

5 Analysis of Results

In this section the results of the measurements are further discussed and compared to the theory of tyre vibration presented in section 3 and to simulation results of the flexible ring model introduced by Gong in 1993 [1]. The flexible ring model was parametrised based on measurement results of the studied tyre and equation 18 presented in section 2.6.1. The measurement results from the different measurements are all considered and compared with each other when possible.

5.1 Static Tyre

All of the vibration measurements performed on a static tyre with and without ground contact resulted in clean mode shapes as was presented in sections 4.3 and 4.4. The theory presents that a static tyre with no ground contact should have two rotating modes at one natural frequency of the tyre forming a standing wave on the tyre. The measurements presented in section 4.3 seem to show what the theory suggests and the modes with circumferential mode numbers varying from 1 to 9 were detected with the FRF and SSI algorithms. Additionally, the first acoustic mode of the tyre was detected at a frequency of 227 Hz when using the SSI algorithm. The similarity of the results from two different identification algorithms and good agreement suggests that the algorithms used in this thesis have been implemented without significant error.

By using equation 22 it is possible to calculate the predicted natural frequency of the acoustic mode of the tyre. By selecting the speed of sound to be 343 m/s, a circumferential mode number of 1 and an air cavity length of 1.568 m, the calculated natural frequency of the cavity is 218.75 Hz. The difference between the measured and calculated acoustic modes is 8.25 Hz and may be explained by the relatively simple model used for the theoretical calculation and error in the measurements.

The damping identified by the SSI algorithm for the acoustic mode is significantly smaller than the corresponding values identified for the other modes. This is likely due to the difference in the propagation medium. The modes travelling in air should have a lower damping than modes propagating through rubber. The difficulty in identifying the acoustic mode using the FRF method is likely due to the accelerometer being attached to the rubber and therefore having much lower amplitudes because the modal coupling between the rubber and the air is quite low.

In section 4.4 the measurements of the same static tyre with a ground contact are presented. A significant 4 kN load imitating the weight of a passenger car was applied to it through the test bench suspension system. The ground contact forced the bottom of the tyre to stay still, which affected the mode shapes and their frequencies. The effect of the loading of the tested tyre on the identified natural frequencies is presented in Table 7. From the comparison between the loaded and free tyre it can be seen that loading the tyre seems to increase the natural frequency of the detected modes for almost all of the modes. The single exception is the first mode which showed a decrease of 8.69 % in the detected natural frequency after loading the tyre. The change was greatest for mode numbers ranging from 4 to 6. The

Table 7: The natural frequencies of the free and loaded tyre. The values with the same circumferential mode numbers are compared and relative differences calculated. The natural frequencies chosen for the comparison were selected from the identification results of the SSI algorithm for both measurements.

Mode number	**Free tyre**	**Loaded Tyre**	**Relative difference**
1	107.0 Hz	97.7 Hz	-8.69 %
2	116.3 Hz	123.0 Hz	5.76 %
3	140.0 Hz	153.0 Hz	9.29 %
4	166.3 Hz	179.8 Hz	8.12 %
5	193.7 Hz	210.0 Hz	8.42 %
6	221.7 Hz	242.4 Hz	9.34 %
7	253.4 Hz	270.8 Hz	6.87 %
8	286.5 Hz	295.0 Hz	2.97 %
1st acoustic	227.0 Hz	230.7 Hz	1.63 %

relative difference in natural frequency between the unloaded and loaded tyre seems to decrease after passing the 250 Hz frequency. The effect of forcing a static point on the tyre may affect the higher mode numbers less because the wave length is much shorter for them and therefore a smaller adjustment of the original shape is needed to have a static point in the bottom of the tyre.

The acoustic mode showed a significantly smaller change than the other modes near the same frequency. The small change may be caused by a decrease in the inner volume and shape of the tyre, but a difference of 1.63 % can also easily be caused by measurement error. The mode shape of the acoustic mode in the tyre with ground contact is more spiky than in the free tyre as can be seen by comparing figures 26 and 29. A possible explanation is that the mode gets coupled with the 6th mode and is therefore harder to detect. The coupling of the acoustic mode with the other tyre modes was considered in section 3.3 and also detected by Kindt in 2009 [10].

Table 8: The measured natural frequencies of a rolling tyre with cleat excitation compared at different rolling velocities.

Mode shape	**20 km/h**	**40 km/h**	**60 km/h**
(2,0)extr.	95.7 Hz	99.0 Hz	-
(3,0)0	122.7 Hz	123.0 Hz	108.8 Hz
(5,0)extr.	134.4 Hz	-	139.0 Hz
(6,0)extr.	181.9 Hz	198.1 Hz	-
(7,0)extr.	209.2 Hz	218.1 Hz	173.6 Hz
(8,0)extr.	-	241.0 Hz	224.4 Hz
(8,0)0	258.6 Hz	-	214.4 Hz
(10,0)extr.	-	303.0 Hz	293.9 Hz
(12,0)extr.	431.1 Hz	-	379.7 Hz
(14,0)extr.	479.9 Hz	484.9 Hz	433.9 Hz

5.2 Rolling Tyre

The modes of the rolling tyre were identified using a timed cleat excitation with varying sensor locations along the tyre as was explained in sections 4 and 4.2. The results of these measurements were presented in sections 4.6.1, 4.6.2 and 4.6.3. Because the excitation changes when the rotation speed increases, the same modes were not always detected in all of the measurements. The natural frequencies of modes that were identified on at least two of the three measurements are listed in table 8. For most of the modes identified the natural frequency seems to increase slightly when increasing the rolling speed from 20 km/h to 40 km/h. However, increasing the speed further to 60 km/h seems to decrease the natural frequencies of the identified modes significantly. This kind of non-monotonic behaviour is quite surprising and casts some doubt on the use of the SSI identification method for a rotating tyre. Nevertheless, it should be taken into account that a comparison of this kind is somewhat hindered by the fact that only three modes with similar shapes were found in all of the measurements. The reliability of the results for the rotating tyre should be questioned because the mode shapes are hard to identify and the natural frequencies of modes with the same mode number do not behave as expected.

From the animations of the measured acceleration it is possible to see that the excitation of the tyre can be divided into three major parts:

1. The initial contact of the cleat with the front edge of the tyre.
2. The enveloping of the cleat.
3. The exit of the cleat from the contact area.

The first of these three almost exclusively excites the front edge of the tyre and therefore most of the waves will travel against the rotation direction of the tyre. The initial contact produces a high acceleration peak in the accelerometer, but the highest value is measured during the second phase of excitation. When rolling at 60 km/h the accelerometer experienced around 3000 g of acceleration in the enveloping phase of excitation. There may, however, be significant error in the peak acceleration value measured as it exceeds the highest rated value of the sensor three times over. In addition to providing the highest acceleration peak, the second phase of excitation affects both sides of the tyre and travelling waves are emitted in both directions around the tyre. The peak acceleration during the last phase of excitation is significantly lower than in the other two phases and it mostly excites the rear edge of the tyre. Because the rear edge of the tyre is excited more, most of the produced waves are forward travelling. The different phases of cleat excitation have been presented in figure 37. The figures do also contain the accelerations caused by the static deformation shape of the tyre.

From the tyre vibration animations it is possible to see that forward and backward travelling waves propagate at different velocities. This is caused by the rotation of the tyre and is expected, but the faster movement speed of forward travelling waves combined with the reflection of waves from the contact patch makes all of the waves travel in one direction. This happens after the fast travelling waves have reflected from the contact patch and the slower travelling waves are still on their way.

From the measurements it was further observed that in addition to the moving impulses clearly visible in figure 37, there are some waves with a significantly higher propagation speed and a lower amplitude. Visually they seem to have a low circumferential mode number from around three to five and can be seen in figure 37b. From the figure it is clearly visible that there is already some vibration at the opposite side of the contact patch even though the main wave is still travelling at the edge of the tyre. The vibrations are quite low amplitude but can easily be seen by comparing the upper side of the tyre in figure 37b to the unexcited upper side of the tyre in figure 37a.

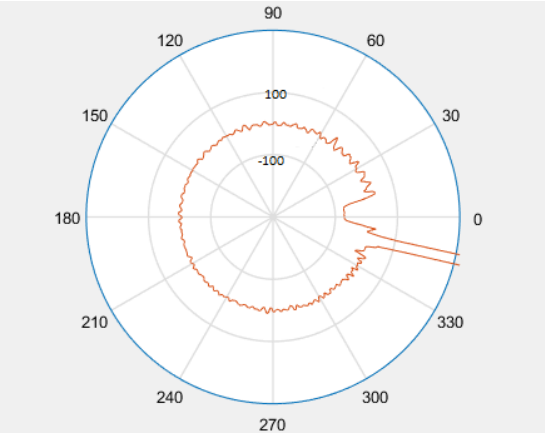

(a) The tyre at the moment of initial cleat contact.

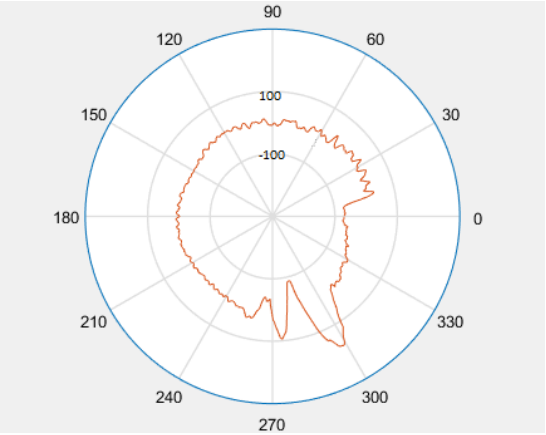

(b) The tyre after the initial contact and before it envelopes the cleat.

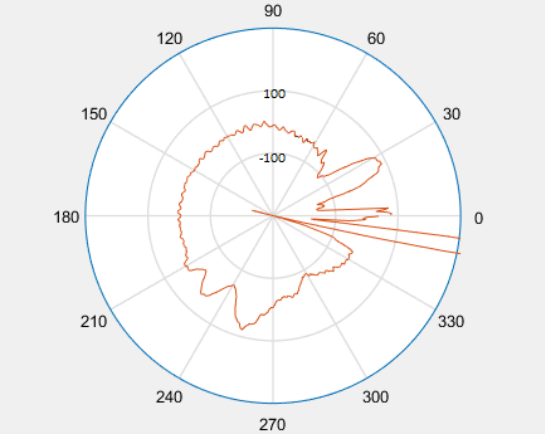

(c) The tyre enveloping the cleat.

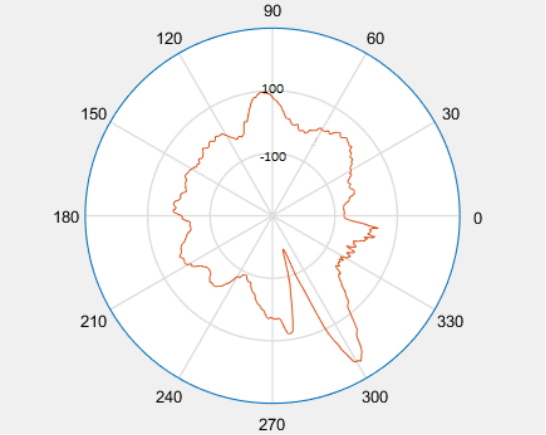

(d) The tyre after it has enveloped the cleat.

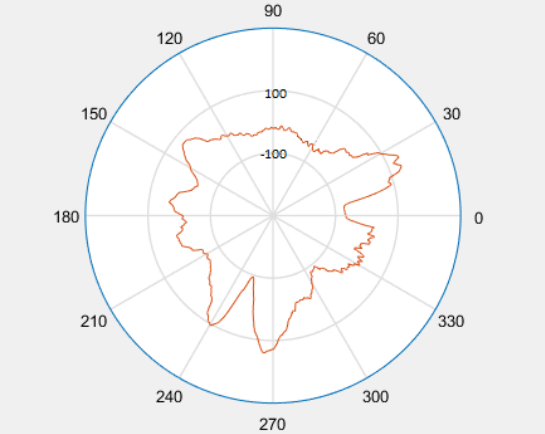

(e) The exit of the cleat from the contact area.

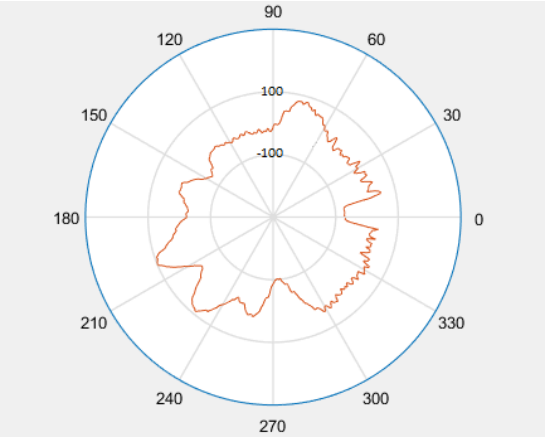

(f) The tyre after the excitation is over.

Figure 37: The radial accelerations of the tyre rubber measured at a few interesting phases of excitation and plotted in polar coordinates. The position of the measurement point is presented as the angle(degrees) of the polar coordinate and the measured acceleration(g) has been fitted to the radial coordinate. The zero angle corresponds to the position of front edge of the contact area and the tyre rotates anticlockwise. Positive accelerations refers to acceleration towards the centre of the tyre. The tyre is rolling at 40 km/h with a 4 kN load.

Table 9: The tyre parameters used for the flexible ring model.

Parameter	Symbol	Value
Tyre inner width	b_0	0.152 m
Tyre air pressure	p_0	2.2 bar
Tyre mass density	ρA	2.715 m^2kg
Damping ratio	λ	2.5%
Treadband radius	R_t	0.296 m
Tread stiffness	k_{trd}	$19{\times}10^6$ N/m^2
Bending stiffness	EI	0.9426 N/m^2
Radial spring stiffness	k_w	$1.294{\times}10^6$ N/m^2
Tangential spring stiffness	k_v	$1.161{\times}10^6$ N/m^2

5.3 Comparison with the Simulated Flexible Ring Model

To compare the measurement results with the flexible ring model, the correct parameters have to be found first. The final values used in the simulations of this thesis for all the tyre parameters can be found from table 9. The tyre inner width was selected by using the value provided be Zegelaar in 1998 for his tyre of the same outer width [3]. The treadband radius was determined by taking the outer diameter of the tyre and deducting 2 cm to compensate for the thickness of the tread pattern and get the radius of the treadband centre. The damping ratio was selected based on the identification result of the free tyre to approximately 2.5%.

The radial and tangential spring stiffnesses and the bending stiffness were determined by solving the values using three detected modes of the tyre and equation 18. The modes selected for these stiffness calculations were (1,0), (3,0) and (7,0) of the static tyre. By using these detected stiffness values it was now possible to predict the natural frequencies of the other detected modes. The tyre mass density was finally iterated to find the value resulting in the lowest summed absolute error of the predicted natural frequencies. The prediction results with the final tyre mass density can be found from table 10.

After being tuned, the flexible ring tyre model does seem to predict the remaining natural frequencies of the free tyre relatively well. The highest relative error in the simulation model is produced in the (2,0) mode. This may be caused by the uncertainty in the low frequency modes used to parametrize the model or error in the natural frequency of the (2,0) mode itself. This conclusion is supported by the fact that the identification results between the SSI and FRF methods on these low frequency modes had quite big differences, as can be seen from table 2. The stabilization diagram presented in figure 24b also shows that the identified frequencies of the (1,0) and (2,0) modes are relatively unstable.

After we have solved the bending stiffness and the radial and tangential spring

Table 10: The natural frequencies of the tyre detected experimentally are compared to the simulation results from the parametrised flexible ring model. The frequencies detected by the SSI method were used for tuning the model. The three frequencies with 0 % relative error were used for finding the spring stiffness values for the model.

Mode shape	**Experimental**	**Simulated**	**Relative error**
(1,0)	107.0 Hz	107.0 Hz	0.0 %
(2,0)	116.3 Hz	119.8 Hz	3.0 %
(3,0)	140.0 Hz	140.0 Hz	0.0 %
(4,0)	166.3 Hz	164.7 Hz	0.98 %
(5,0)	193.7 Hz	192.3 Hz	0.72 %
(6,0)	221.7 Hz	222.0 Hz	0.15 %
(7,0)	253.4 Hz	253.4 Hz	0.0 %
(8,0)	286.5 Hz	286.2 Hz	0.11 %
(9,0)	320.3 Hz	320.3 Hz	0.0017 %

stiffnesses the only parameter still to be solved is the stiffness of the secondary spring. This parameter is needed to use the model of a rolling tyre on flat road derived by Gong in 1993 [1]. The simulation results from this model can be quite easily compared to the acceleration measurements of a rolling tyre on a smooth drum, but the simulation model doesn't account for the attenuation of the shapes while they propagate around the tyre.

The best value for the secondary spring stiffness was selected by iterating through a range of values and running the model with all of them. All of the simulation results were compared against the measurements of a real tyre rolling with same speed on a flat drum and the secondary spring stiffness producing the lowest simulation error was selected. The rolling speed selected to find the correct value was 50 km/h. Other rolling velocities resulted in only slightly different values.

To compare the simulation results with the accelerometer measurements, the displacements provided by the simulation had to be converted to acceleration values of a scanning accelerometer. This was performed by first calculating the second derivative of the displacements and then resampling to equal sample rate.

The simulation and measurement results at different velocities can be seen in figure 38. In figures 38a and 38b there is a sine wave pattern clearly visible in the experimental measurements. The pattern is caused by the Earth's gravitational field and is present in all of the measurements, but it is harder to observe when the rolling speed increases. From figure 38 it is possible to see that the flexible ring model produces approximately the correct shapes, especially near the ground contact patch. However, it seems to be unable to produce the smaller and higher wave number vibrations measured by the sensor. These vibrations can't be measurement noise because they appear the same over multiple rotations as was shown in figure 22.

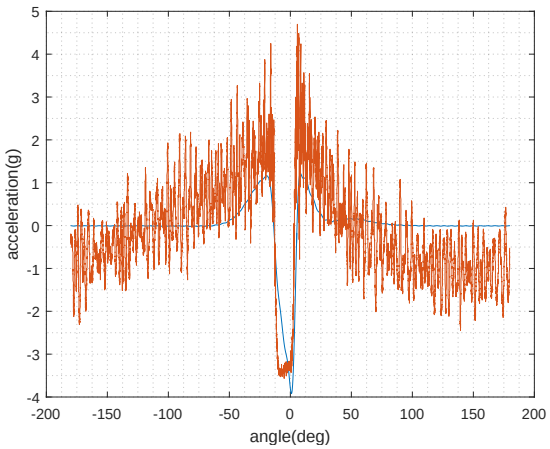

(a) Radial acceleration at 10 km/h.

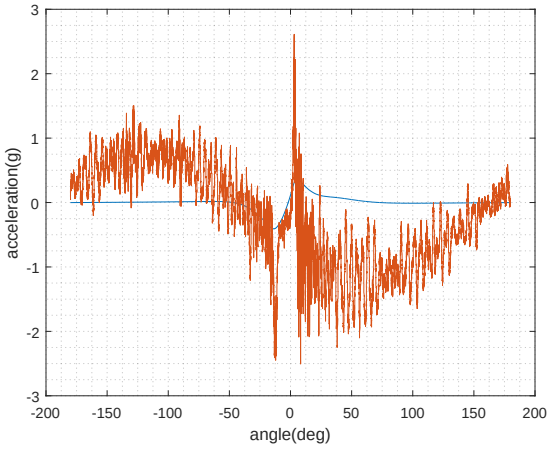

(b) Tangential acceleration at 10 km/h.

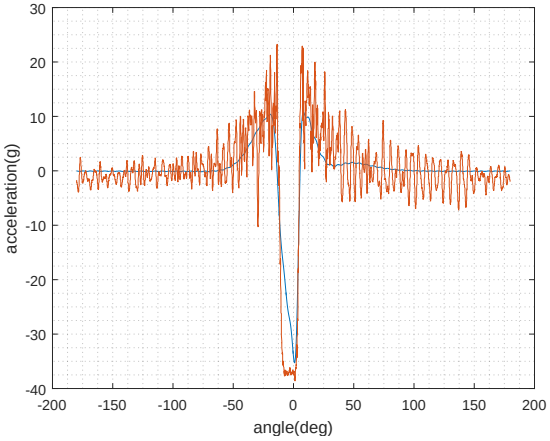

(c) Radial acceleration at 30 km/h.

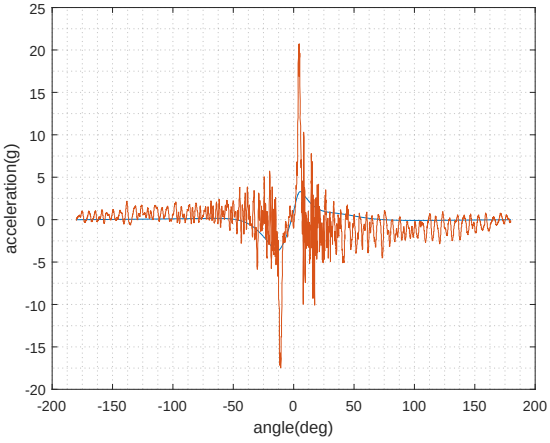

(d) Tangential acceleration at 30 km/h.

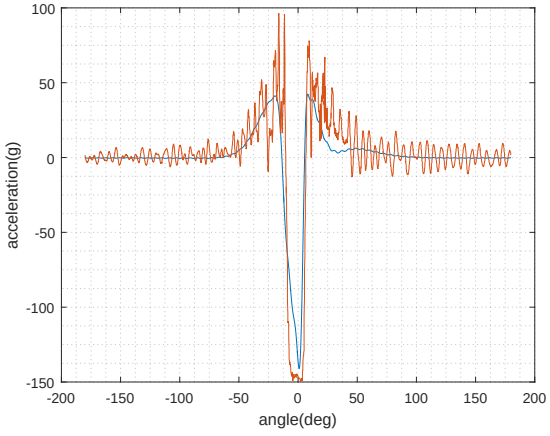

(e) Radial acceleration at 60 km/h.

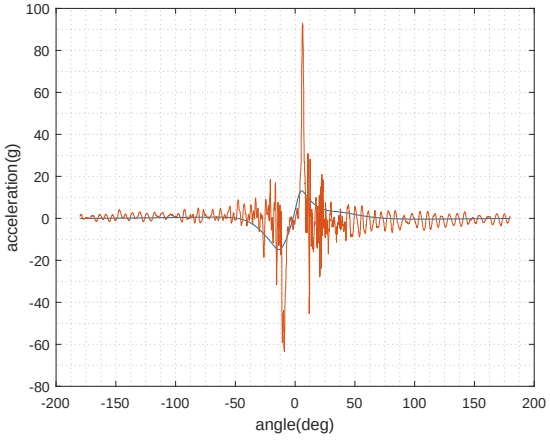

(f) Tangential acceleration at 60 km/h.

Figure 38: The measured(orange line) and simulated(blue line) acceleration values at different rotation speeds plotted as the function of sensor angle.

Instead, they are caused by the actual deformation of the tyre treadband and should be produced by a good enough tyre model. Additionally, the simulation model is unable to produce the high tangential acceleration peaks at the edges of the contact area.

The flat area in the middle of the contact patch as seen in the real measurements is caused by the accelerometer rotating to become parallel with the ground. Therefore the radial and tangential components of the tyre are no longer completely radial or tangential in the measurements. Because this doesn't happen in the simulations, there are some differences between the shapes of the acceleration curves between the measurements and simulation at the contact area.

6 Conclusions

In this thesis some methods for identifying the modal parameters of a tyre were first presented. Calculating the FRF of the tyre by using the measured force input and the tyre acceleration measurements is the traditional method used for the modal analysis of structures. The FRF can be used to detect to modes of the tyre, if the input force is measured. By using the SSI method it is possible to detect the modal parameters of the tyre without measuring the input force. Therefore, SSI is much easier to apply for the identification of the modes of a rotating tyre, where measuring the input force can be more difficult.

Later the structure of the modern radial ply tyre and a classification for the tyre modes were presented. The formation of the standing waves and the cavity resonances on a static tyre were explained. The effects of rotation on a car tyre were considered and summed up. The rotational stiffening, bifurcation of natural frequencies and Doppler shift should explain most of the differences between a rotating and a static tyre.

The tyre vibrations were measured in four different cases: A static tyre without ground contact, a non-rotating tyre with ground contact, a rolling tyre on flat surface and a rolling tyre with cleat excitation. The measurements with a non-rotating tyre showed a good agreement on the detected mode shapes when comparing the results of the SSI and FRF identification algorithms. Additionally, the detected mode shapes for the static cases were as one would expect based on the tyre vibration theory.

No method was found to identify the modes of the rotating tyre without cleat excitation, because the acceleration measurements always showed the same value with the same position of the sensor on the tyre. However, the tyre showed an interesting static acceleration pattern, which was detected because the accelerometer moved through the tyre. It may be possible in the future to identify different changes in the rolling conditions based on the change of this pattern. These measurements were used together with the static tyre measurements to parametrize a steady state flexible ring model of a rolling tyre on flat road. The parametrised model was compared with the measurements and it was concluded that the model was able to model the general shape of the tyre, but much of the measured higher frequency vibration couldn't be found from the parametrised model.

The natural frequencies and mode shapes detected from the rotating tyre measurements with cleat excitation varied quite significantly between different rolling speeds due to the change in the excited frequencies with a faster moving cleat. There were also difficulties in meaningfully visualizing the identification results because of the increased complexity of the mode shapes in the rotating tyre. A more suitable identification and visualizing method might improve the results of the mode detection. In addition animations were created of the tyre radial acceleration after the cleat impact. These animations clearly revealed that the cleat excitation comprised of multiple phases and how the impulses travel around the tyre at different velocities.

The high resolution and high consistency of the measurements created from multiple excitations help to show that only a single embedded accelerometer can be used to precisely measure tyre vibration by using the method presented in this thesis.

By continuing the test for a longer time, the position resolution of the measurement could further be increased, and by deploying multiple accelerometers side by side at the same tyre angle, a more comprehensive measurement result could be achieved. These kinds of high resolution measurements are necessary in developing accurate tyre models capable of reproducing the high frequency behaviour of the car tyre. In the future, a model of the tyre could first be identified using the cleat experiment and later the same model could be used to estimate the complete state of the tyre based on measurements of a single accelerometer.

References

[1] S. Gong. *A Study of In-Plane Dynamics of Tires*. PhD thesis, Delft University of Technology, 1993.

[2] S. Kim and A. Savkoor. The Contact Problem of In-Plane Rolling of Tires on a Flat Road. *Vehicle System Dynamics*, 27:189–206, 1997.

[3] P. Zegelaar. *The Dynamic Response of Tyres to Brake Torque Variations and Road Unevennesses*. PhD thesis, Delft University of technology, 1998.

[4] J. Périsse. A Study of Radial Vibrations of a Rolling Tyre for Tyre–Road Noise Characterisation. *Mechanical Systems and Signal Processing*, 16(6):1043–1058, 2002.

[5] K. Iwao and I. Yamazaki. A Study on the Mechanism of Tire/Road Noise, 1996.

[6] A. Niskanen and A. Tuononen. Three 3-axis Accelerometers Fixed Inside the Tyre for Studying Contact Patch Deformations in Wet Conditions. *Vehicle System Dynamics*, 52(sup1):287–298, 2014.

[7] A. Tuononen. Optical Position Detection to Measure Tyre Carcass Deflection. *Vehicle System Dynamics*, 46(6):471–481, 2008.

[8] R. Matsuzaki and A. Todoroki. Intelligent Tires Based on Measurement of Tire Deformation. *Journal of Solid Mechanics and Materials Engineering*, 2(2):269–280, 2008.

[9] J. Holtschulze, H. Goertz, and T. Hüsemann. A Simplified Tyre Model for Intelligent Tyres. *Vehicle System Dynamics*, 43(sup1):305–316, 2005.

[10] P. Kindt. *Structure-Borne Tyre / Road Noise due to Road Surface Discontinuities*. 2009.

[11] B. Schwarz and M. Richardson. Experimental Modal Analysis. In *CSI Reliability Week, Orlando, FL*, pages 1–12, 1999.

[12] G. Kerschen and J. Golinval. Experimental Modal Analysis.

[13] P. Van Overschee and B. De Moor. Subspace Algorithms for the Stochastic Identification Problem. In *Proceedings of the 30th Conference on Decision and Control*, 1991.

[14] B. Peeters and G. De Roeck. Reference-Based Stochastic Subspace Identification Method for Output-Only Modal Analysis. *Mechanical Systems and Signal Processing*, 13(6):855–878, 1999.

[15] E. Reynders, R. Pintelon, and G. De Roeck. Uncertainty Bounds on Modal Parameters Obtained From Stochastic Subspace Identification. *Mechanical Systems and Signal Processing*, 22(4):948–969, 2008.

[16] K. Arun and S. Kung. Balanced Approximation of Stochastic Systems. *SIAM. J. Matrix Anal. & Appl.*, 11(1):43–68, 1990.

[17] H. Van Der Auweraer and B. Peeters. Discriminating Physical Poles From Mathematical Poles in High Order Systems: Use and Automation of the Stabilization Diagram. In *Conference Record - IEEE Instrumentation and Measurement Technology Conference*, volume 3, pages 2193–2198, 2004.

[18] I. Goethals and B. De Moor. Model Reduction and Energy Analysis as a Tool to Detect Spurious Modes. In *Proceedings of the 2002 International Conference on Noise and Vibration Engineering, ISMA*, number 1, 2002.

[19] J. Mark, B. Erman, and M. Roland. *The Science and Technology of Rubber*. Academic press, 2013.

[20] R. Wheeler, H. Dorfi, and B. Keum. Vibration Modes of Radial Tires: Measurement, Prediction, and Categorization Under Different Boundary and Operating Conditions. Technical report, SAE Technical Paper, 2005.

[21] K. Larsson and W. Kropp. A High-Frequency Three-Dimensional Tyre Model Based on Two Coupled Elastic Layers. *Journal of Sound and Vibration*, 253(4):889–908, 2002.

[22] R. Pinnington and A. Briscoe. A Wave Model for a Pneumatic Tyre Belt. *Journal of Sound and Vibration*, 253(5):941–959, 2002.

[23] J. Thompson. Plane Wave Resonance in the Tire Air Cavity as a Vehicle Interior Noise Source. *Tire Science and Technology*, 23(1):2–10, 1995.

[24] I. Lopez, R. Blom, N. Roozen, and H. Nijmeijer. Modelling Vibrations on Deformed Rolling Tyres-A Modal Approach. *Journal of Sound and Vibration*, 307(3-5):481–494, 2007.

[25] Y. Kim and J. Bolton. Effects of Rotation on the Dynamics of a Circular Cylindrical Shell with Application to Tire Vibration. *Journal of Sound and Vibration*, 275(3-5):605–621, 2004.

[26] R. Matsuzaki and A. Todoroki. Passive Wireless Strain Monitoring of Actual Tire Using Capacitance-Resistance Change and Multiple Spectral Features. *Smart Materials and Structures*, 14(4):561–568, 2005.

[27] R. Matsuzaki and Ak. Todoroki. Wireless Flexible Capacitive Sensor Based on Ultra-Flexible Epoxy Resin for Strain Measurement of Automobile Tires. *Sensors and Actuators*, 140(1):32–42, 2007.

[28] A. Niskanen and A. Tuononen. Three Three-Axis IEPE Accelerometers on the Inner Liner of a Tire for Finding the Tire-Road Friction Potential Indicators. *Sensors (Switzerland)*, 15(8):19251–19263, 2015.

[29] J. Cho, K. Kim, and H. Jeong. Numerical Investigation of Tire Standing Wave Using 3-D Patterned Tire Model. *Journal of Sound and Vibration*, 305(4-5):795–807, 2007.

[30] W. Soedel. On the Dynamic Response of Rolling Tires According to Thin Shell Approximations. *Journal of Sound and Vibration*, 41(2):233–246, 1975.

[31] A. Chatterjee, J. Cusumano, and J. Zolock. On Contact-Induced Standing Waves in Rotating Tires: Experiment and Theory. *Journal of Sound and Vibration*, 227(5):1049–1081, 1999.

[32] Endevco Corporation. Model 35A Isotron ® accelerometer Datasheet.

[33] H. Pirjola. Development of Tyre Force Measuring Device. Master's thesis, Helsinki University of Technology, 2001.

[34] M. Imregun and D. Ewins. Realisation of Complex Mode Shapes. *Proceedings of the IMAC XI*, 2:1303–1309, 1993.